A STUDY OF MESOSCALE SIMULATIONS FOR PLANAR SHOCK EXPERIMENTS ON HETEROGENEOUS GRANULAR MATERIALS

by

Merit G. Schumaker, B.S.

A Thesis submitted to the Faculty of the Graduate School,
Marquette University,
in Partial Fulfillment of the Requirements for
the Degree of Master of Science

Milwaukee, Wisconsin

May 2015

ABSTRACT
A STUDY OF MESOSCALE SIMULATIONS FOR PLANAR SHOCK EXPERIMENTS ON HETEROGENEOUS GRANULAR MATERIALS

Merit G. Schumaker, B.S.

Marquette University, 2015

There is an interest in producing accurate and reliable computer simulations to predict the dynamic behavior of heterogeneous materials and to use these simulations to gain further insight into experimental results. In so doing, a more complete understanding of the multiple-length scales involved in heterogeneous material compaction can be obtained. Mesoscale computer simulations of dynamically shocked materials have proven to be a beneficial resource in unraveling data not observed in planar shock impact experiments, such as stress and temperature interactions between grains.

The modeled mono-dispersed geometry of particles, the densities of each material, equations of state, material properties and many other factors affect the simulated outcomes. By studying and analyzing these variables, many of which highlight the difference between experimental and simulated results, there manifests additional insight into the shock dynamics of the different heterogeneous granular materials. The heterogeneous materials in this study were created both by a "shake and pack" method, where individual grains were randomly seeded into the computational domain and grown until the grains matched the experimental volume fraction and average diameter.

Three planar shock experiments were utilized to validate simulation models and parameters: 1. Brake pad powder compaction at Marquette University, 2. Dry sand experiments at Georgia Tech, and 3. Release of dry sand at Cambridge University. Planar shock impact experiments were simulated using two different hydrocode packages: CTH and iSALE. Validated models are then used to setup future dry, water, and possible ice saturated sand release experiments. Particle velocity and stress traces obtained from the computer simulations were compared to VISAR, PDV, and Manganin gage measurements obtained from experiments. The results from simulations are compared to experiments and discussed in this document.

ACKNOWLEDGMENTS

Merit G. Schumaker, B.S.

Although I will never be able to quite acknowledge everyone for his or her help and guidance, I nonetheless wish to extend my appreciation to:

God, for her guidance and the strength she has given me through these last six years at Marquette,

My committed family who have supported my goals of obtaining a higher education,

My best friend and girlfriend, Jenifer Wolin, for all of her love and kindness to get me through the toughest of times,

My close friends and engineering colleagues, for all of the laughs and endurance through the late nights,

The brothers of the Xi-Xi chapter of the Kappa Sigma Fraternity,

My advisor, Dr. John P. Borg, for his wisdom and knowledge in developing my professional skills as well as my understanding in shock physics and mechanical engineering,

Dr. Naresh Thadhani and Dr. Gregory Kennedy from Georgia Tech, Dr. Sarah Stewart from Harvard University, and Dr. Christopher Braithwaite from Cambridge University in the UK for all of their help and experimental expertise,

The Air Force Office of Scientific Research for their grant support,

And last, but definitely not least, the Marquette University administration and faculty.

TABLE OF CONTENTS

LIST OF TABLES

LIST OF FIGURES

LIST OF EQUATIONS

I. INTRODUCTION

1.1 Motivation

The Air Force Office of Scientific Research (AFOSR) in cooperation with Georgia Tech, Harvard University, and Marquette University is interested in further understanding the dynamic response of granular materials by the use of mesoscale simulations for planar shocked heterogeneous granular materials. There is quite a wide range of applications in the compaction and shock compression of granular materials; from researching how bullets and grenade blasts affect sandbags on the battlefield, investigating the asteroid impacts on our planet and in the universe [1], and describing how particles arrange themselves in ways that are more favorable to absorb energy when subjected to certain frequencies [2], there exist opportunities to theoretically model the non-linear shockwave phenomena of granular materials and unravel the multiple-length scale information involved in heterogeneous material compaction.

Other interests in the field of shock compaction of heterogeneous materials include the study of shock properties of concrete [3], where sand and other types of aggregates are added to strengthen and bind concrete. Specifically, the properties of the sand in concrete are of interest when the destruction of ordinance and landmines or the penetration of projectiles into sand is considered [4, 5]. Even the recent Anthrax scare of the early 2000s at the Capitol in Washington DC, dealt with understanding how sand particles a few microns in diameters could better package the Anthrax pathogen; this particular type of research actually dates back to World War II when "dirty" bombs were

dropped on axis powers from Russia, which utilized quartz particles to spread pathogens [6].

Different mixtures of concrete, including but not limited to the amount of water, rebar or steel fibers, and the size of the sand aggregate change the yield strength of the overall bulk material. Not only is this of interest to protecting soldiers but it also helps to characterize the types of weapons needed in order to penetrate an enemy's bunker or structure. Before understanding the bulk properties of a concrete mixture, the individual constituents are just as important in painting an overall picture of the shock physics of heterogeneous granular materials. This document in particular will focus on two types of heterogeneous granular materials: dry sand of various densities and sizes and a brake pad powder mixture consisting of six different materials.

Although there have been numerous experiments and computer simulations investigating the dynamic behavior of dry sand [4, 7-13] and some other heterogeneous granular mixtures [1, 14-21], there are still ample opportunities for improvement of models and setting up simulations for heterogeneous materials.

The types of computer simulations presented in this document are known as mesoscale, which branches between macro and micro scales. The computational domain is typically no larger than 2 cm in the direction of shock and 5 mm in the latitudinal directions. Grain sizes range from 75 microns up to 500 microns, with volume fractions ranging from 50 percent to more closed packed sands of 70 percent. Mesoscale simulations bridge the gap between treating a material as a homogenous and applying a porosity model to it, and observing individual particle properties during a shock event. These types of simulations help to better characterize complicated heterogeneous

materials, such as brake pad powders, water saturated sand, and ice sand mixtures, where simply treating these types of material compositions as a bulk, homogenous material would be oversimplifying the problem at hand.

There are current applications where mesoscale simulations have not been utilized, such as looking at the influence of water on the constitutive behavior of quartz based sand in regards to the blast response of a rigid target [22]. These types of simulations could potentially help to understand how explosives interact on rigid plates in different mediums, such as how an Improvised Explosive Device (IED) effect on a vehicle subject to an explosion. By adding water into the sand and observing the behavior of the shockwave, it helps to not only better characterize sand with water, information that could then be used to protect the lives of soldiers in harm's way. Existing simulations treat the material as a continuum. Mesoscale simulations prevent the computational domain becoming exceedingly large, and in the end helps to better characterize the dynamic shock response of granular materials.

Although the results of a blast response on a rigid target will not be simulated in this document, it's the fact that there are similar simulations and material characterization that solidifies the research in this document. Most computational results are presented in comparison with experiments and help to validate the simulations. Simulations can also provide other results, such as real time shock temperature and stress response for individual particles, which are not found in current experiments [23], and obtain material release information provided by developing isentropic release paths [9].

It is debated if mesoscale simulations produce more reliable and accurate results in comparison to bulk, homogenous simulations. This document shows that there is not

only reliability in comparing experiments to mesoscale simulations, but also more information to be obtained from observing interactions between individual particles.

The interactions of particles and the intensive properties associated with each particle under shock loading, such as temperature, pressure and density, provide insight into how collections of particles behave when loaded. As will be discussed from some of the findings in this document, not all of the particles subjected to impact loading actually reach a state of shock; there are a certain number of particles that are unaffected by shock loading entirely. It has even been suggested that particles of any medium arrange themselves in a manner that the greatest amount of energy dissipation can occur [2]. In order to quantify this energy dissipation, typically in the form of heat, entropy generation would have to be calculated. The simulations in this document do not resolve the surfaces of grains, so the forces and frictions between the grains cannot be calculated. Neglecting these particular factors introduces errors in the estimation of heat release and entropy generation.

The simulated results shown in this document provide novel insights into the shockwave compaction of heterogeneous granular materials and provide theoretical insight into heterogeneous granular materials, specifically the interaction of particles, such as dry sand and brake pad powders. Experiments have tested and produced shock response data corresponding to the bulk response of a material, but not been able to record shock states of individual particles.

1.2 Problem Description

There are three simulations to be described and presented in this document, all of which provide unique and new results in the area of shock compaction of granular materials. These three simulations are located below in table 1.1.

Table 1.1 List of Simulated Experiments

University	Type of Experiment	Material	Reference
Marquette	Dynamic Compaction	Brake-Pad Powder	[23]
Georgia Tech	Planar Shock	Dry Sand	[24]
Cambridge, UK	Planar Shock with an emphasis on Release	Dry Sand	[9]

The shock stress regime for each of these experiments is between 1 and 4 GPa and does not require complicated equations of state, since the phase transition of quartz will not be considered in this document [25], as will be discussed in the section on *Flyer Plate Case Studies*. CTH provides spatial state variable data inside the target domain, which can provide stress and temperature distributions of individual particles, some at the Hugoniot state and others not quite at the same state.

The brake pad simulations accomplished at Marquette University by Cullen Braun provide a foundation of how stress and temperature distributions of individual constituents should be presented in order to apply the same methods for future water and ice sand mixtures [23].

The two types of hydrocode software utilized in the analysis are iSALE and CTH. iSALE is a hydrocode maintained by Museum für Naturkunde, Berlin and Imperial College of London. iSALE, like CTH, is an arbitrary Lagrangian Eulerian (ALE) hydrocode, however it is open source and does not require a background check in order to utilize the hydrocode [26, 27]. In this document, iSALE was only used to simulate the planar dynamic bulk response of dry sand at Georgia Tech in two-dimensions. A better understanding of its capabilities is defined in *Chapter 4, section 4.2 Georgia Tech (Dry Sand)*.

The software mainly utilized to model the three experiments above is another ALE hydrocode known as CTH, version 10.3 [28]. CTH was developed by Sandia National Laboratories in Albuquerque New Mexico in 1987, a three dimensional improvement from its predecessors, the one-dimensional code CHARTD made in 1969 and the two-dimensional code CSQ made in 1975, written by Samuel L. Thompson [29].

CTH is known as a *hydrocode* because of the way materials act much like a fluid in the regime of shock, where only compressive stress and strain are considered [30]. However, this is a misnomer, since the materials do not specifically act like an inviscid fluid, but rather as a solid with varying yield strength models [31].

Information from CTH is extracted by the use of tracers, which are placed in the computational domain at the user's discretion where state variables at the location can be recorded. Typically the location of these tracers mimics the location of data acquisition in experiments and writes stress, temperature, particle velocities and other information to an ASCII file. These tracers will be discussed in greater detail in the *Computational Setup* section.

CTH has been designated Export Control Information (ECI), which requires a signature of International Traffic in Arms (ITAR) agreement form and was run remotely from Marquette on an Engineer Research and Development Center Supercomputing Resource Center (ERDC DSRC) Cray XE6 (Garnet), which is the largest unclassified supercomputer in the Department of Defense (DOD) [32]. In order to run the code remotely on Garnet, a National Agency Check with Inquiries (NACI) was required. This allows for students and faculty of academia to access Garnet remotely with what is known as a Yubi-Key, an electronic key developed by Lockheed martin.

Before simulations can be setup for materials with little to no shock response information, modeling of past experiments as well as understanding various methods for modeling the shock response of granular materials should be done first. This is to establish a foundation of what works and does not work in regards to what assumptions should be made in setting up these simulations. Some questions include: How do particles interact with one another? Do these particles work by "welding" (stiction) or sliding against one another? What types of fracture mechanics are applied to the individual grains? How does grain size affect simulations and how should grains be packed and orientated in a simulation's domain? And what material properties and strength models are appropriate for these simulations? These variables present problems in predicting experiments and more importantly modeling the materials that are inserted into the computational domain.

These types of sensitivity simulations have already been completed, specifically with the utilization of mesoscale CTH simulations for dry granular materials [33]. By varying each factor, such as the size of the grain, the dynamic yield strength of the

individual grains, and the volume fraction of the material, sensitivity of the changing factor on the output could be determined [34]. The sensitivity results will be discussed in the *Computational Setup* section in order to give insight into how to correctly model experiments.

The simulated results are not regarded as a method for replacing planar shock experiments, but rather be a supplement in providing results that are not possible from experiments and to validate the experimental results. Planar shock experiments provide needed validation cases for computationalists to setup future simulations that may then offer advanced predictive capabilities and facilitate experiment planning to reduce the number of experiments required to observe fundamental physics in shock loading.

II. SHOCK PHYSICS INTRODUCTION

2.1 Background and Methodology

Shock physics is the study of how materials behave in regimes where only compressive stress and strain are considered to be orders of magnitude greater than the yield stress, which can then be neglected [30]. A typical stress-strain curve is shown below in figure 2.1.

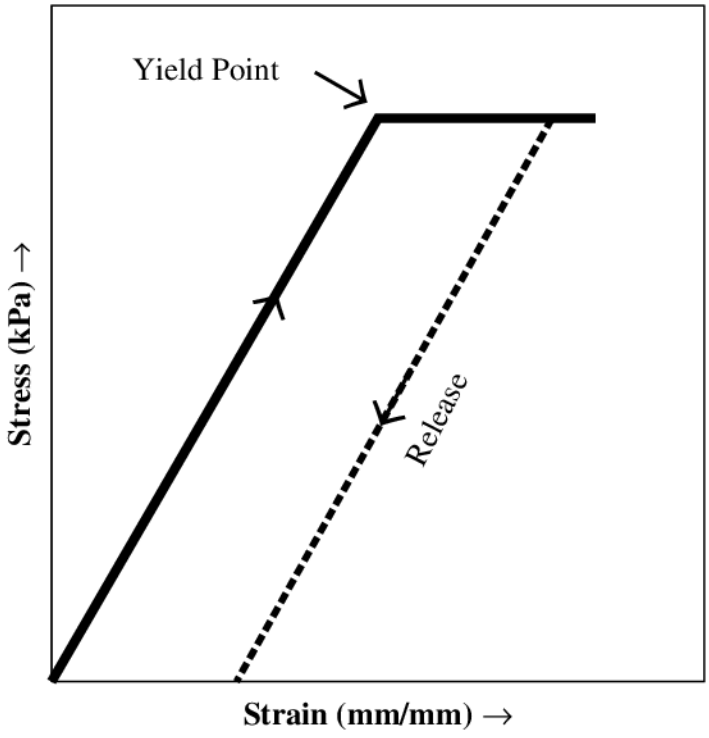

Figure 2.1 General Stress-Strain Plot

Figure 2.1 shows that a material behaves linearly when loaded, either in tension or compression, and will not return to its original shape when loaded past the elastic limit, or the yield point. Permanent plastic deformation occurs when the material is released after the yield point has been exceeded. This is denoted as "release" in figure 2.1, which presents elastic, perfectly plastic profile in tension.

A good example of this behavior is observing a specimen being loaded in uniaxial tension, where a material sample is subjected to a load until the material fails. From these results, a given material can be characterized by specific mechanical properties such as Young's modulus, yield strength, and ultimate tensile strength [35]. The region of stress accessible in typical uniaxial tension experiments is on the order of megapascals (10^6 Pa) for strain rates ranging from 10^{-8} s^{-1} to 10^{-3} s^{-1} [36].

Planar shock experiments access a different stress state than that encountered in a tensile test machine. The planar shock experiments observed in this document utilize gas and powder guns to accelerate a projectile down a barrel with a bore ranging between 25-100 mm in diameter. Gas and powder guns allow for higher regions of stress to be analyzed on the order of gigapascals (10^9 Pa) and are capable of strain rates from 10^3 s^{-1} to 10^5 s^{-1}. The strain state in materials subjected to plate impact is assumed to be one-dimensional strain [36].

Gas guns operate by suddenly releasing compressed gas to accelerate a projectile. Depending on what type of gas is compressed, various speeds can be obtained; for example, if a light gas like helium is utilized in the gas gun breech, the projectile can obtain velocities over 1 km/s, since the gas can expand at a faster rate than heavier gases [37]. Marquette University currently utilizes a ½ inch barrel gas gun for both planar

shock experiments and penetration experiments, with a new 2-inch bore gas gun currently in construction. Gas guns are relatively cheap compared to powder guns, but this can vary depending on the type of gas that is utilized in compression of the breech.

Powder guns, like the one that is shown in figure 2.2 from Eglin Air Force Base near Destin Florida, allow for impact velocities of 2.3 km/s, with peak shock stresses of 100 GPa in materials.

Figure 2.2 Eglin Air Force Research Laboratory (AFRL) HP3 Facility
(Courtesy: Brad Martin, Ph.D. at AFRL)

These types of guns require trained technicians to load the gun breech with gunpowder and follow various sets of procedures to ensure the safety of experimenters [37]. Setups for the target are fairly similar for most planar shock experiments. Figure

2.3 shows a typical target setup from an example of a sand release experiment done by Cambridge.

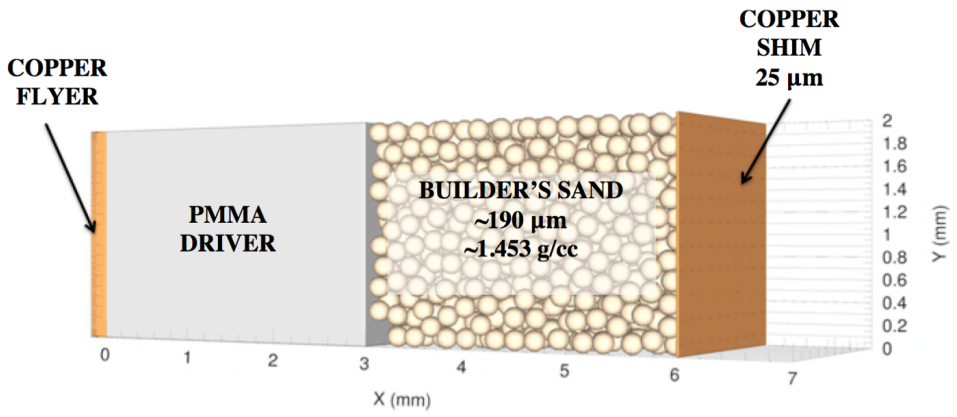

Figure 2.3 Example of an Experimental Setup

Figure 2.3 shows a copper flyer impacting a PMMA driver that drives a planar shock wave into the material of interest (in this case Builder's Sand), and a copper shim. In this particular setup, there is a manganin gage in the PMMA driver, which measures pressure and a laser data acquisition device on the back copper surface to measure particle velocity, known as Photon Doppler Velocimetry (PDV). These setups vary slightly on how data is collected, but the overall setup is quite similar for planar shock experiments. Not to be confused with particle velocity or shock velocity, the impact velocity is associated with the flyer in the experiment and is utilized as part of the initial values in impedance matching, which is discussed later in this section. PDV and the Manganin Gage will be discussed in more detail in section *2.3 Experimental Data Acquisition*.

When a material is subjected to shock, there are three possible different regions of stress strain, as presented in figure 2.4.

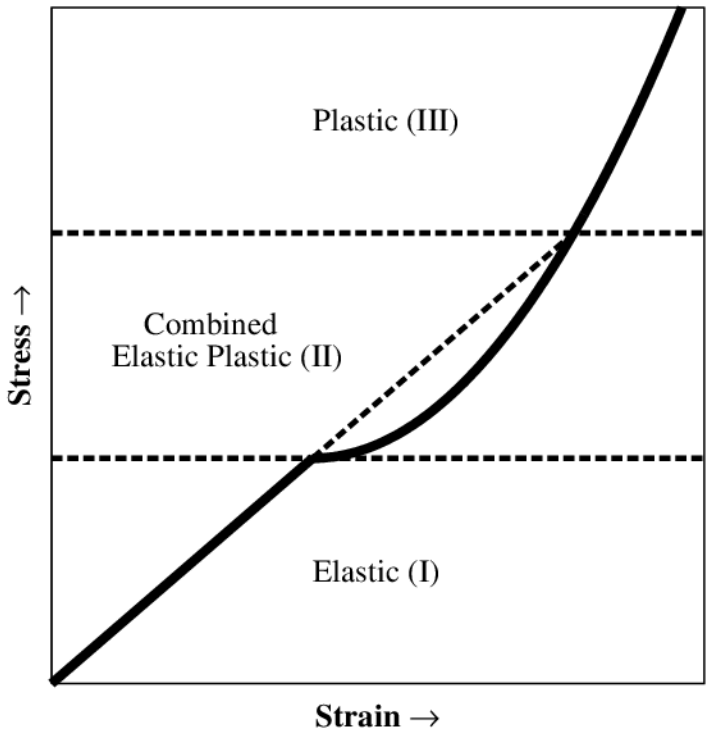

Figure 2.4 Compressive Stress-Strain Curve

In the elastic region of shock, section I in figure 2.4, the sound speed of the material is constant, and is proportional to the change in pressure with change in density [30]. After the elastic region, the combined elastic-plastic portion of the graph, section II, introduces other factors. The factors include, but are not limited to, particle velocity and shock velocity, since the material possesses both an elastic and plastic behavior. Section III is known as the plastic region, where the material does not exhibit any strength.

The particle velocity is the velocity of the already shocked material, or the local material speed, and the shock velocity is the velocity of the propagation of the discontinuity caused by a jump in stress from a reference stress to a shocked stress state [37]. This explanation of particle and shocked velocity is shown illustratively with a car crash test in figure 2.5, where U_p and U_s is the particle and shock velocity, respectively, ρ is the density, P is the stress, and E is the energy. The states 1 and 0 correspond to shocked and unshocked, respectively.

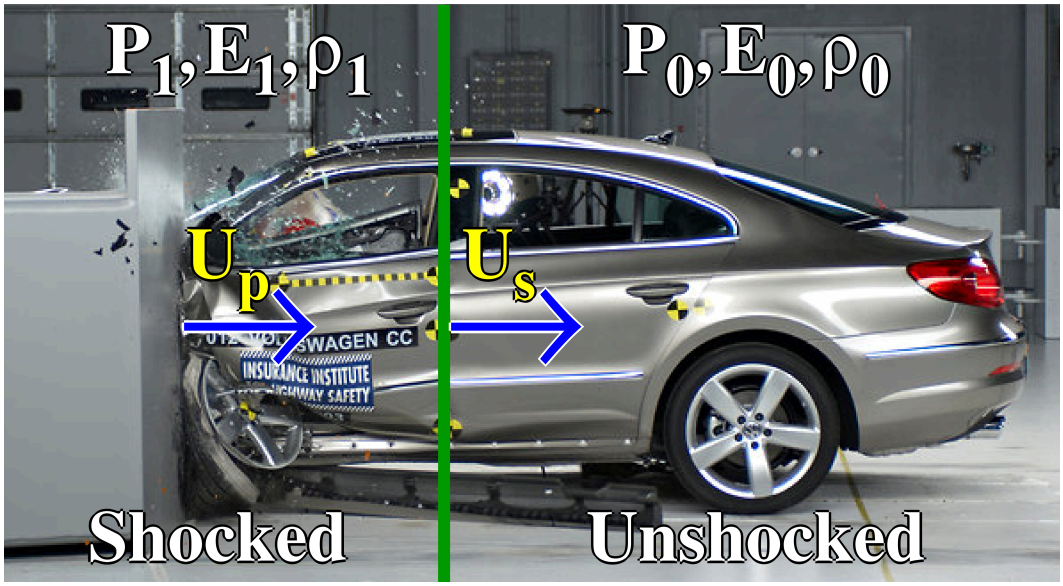

Figure 2.5 Shock Physics Example: Car Crash Test
(Car Test Photo, courtesy of the New York Times)

Car crash tests are relatively slow in comparison to the planar shock experiments simulated in this document. Car crash experiments range from 20 kph up to 130 kph where the planar shock physics experiments in this document have an impact velocities

from 360 kph (100 mps) to 3600 kph (1000 mps). However, figure 3.5 illustrates an applicative use for shock physics and explains the concepts of particle and shock velocity well. Notice that U_p is the particle velocity of the already shocked material and U_s is the velocity of the shock wave traveling through the unshocked material.

Particle (U_p) and shock velocity (U_s) are important in analyzing a material as these values can be substituted into the conservation equations to give information about mass (ρ), momentum (ρu), and energy transfer (E).

In order to characterize a shock wave, the conservation equations are utilized to relate the particle and shock velocity to independent variables, like stress and internal energy. The conservation equations in Eulerian coordinates can be written [37]:

Mass: $$\frac{\rho_o}{\rho} = 1 - \frac{(u - u_o)}{(U - u_o)}, \tag{2.1}$$

Momentum: $$P - P_o = \rho_o(u - u_o)(U - u_o), \tag{2.2}$$

Energy: $$E - E_o = \frac{1}{2}(P + P_o)(V_o - V). \tag{2.3}$$

U and *u* corresponds to shock and particle velocity, respectively. Equations 2.1-2.3 are known as the Rankine-Hugoniot jump conditions, since it relates an unshocked material to a shocked material through a "jump" from a reference state to a shocked state; the shocked state is also known as the Hugoniot state. Again, these relationships can be applied to both two-dimensional and three-dimensional setups, since the wave is assumed

to be planar, meaning that the shock wave traversing the material is a plane instead of a line for three-dimensions. The Hugoniot of a given material is developed from experiments, where the Hugoniot is determined by finding the parameters of a linear fit of a U_s versus U_p, where each data point represents a new shot. Figure 2.6 below shows an example shock Hugoniot for solid quartz.

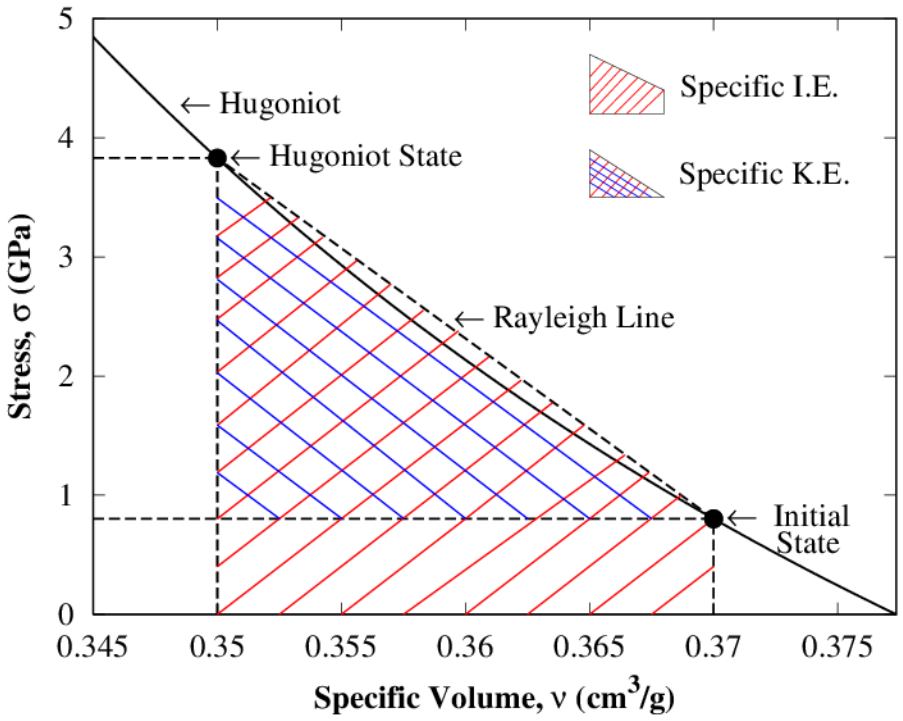

Figure 2.6 Solid Quartz Hugoniot

The Rayleigh line is the path from a reference state to a Hugoniot state. Theoretically, the Rayleigh line defines the jump from the initial state to the shocked state and the Hugoniot represents a locus of shock states a material might achieve based

on the slope of the Rayleigh line. The theoretical isentropic release of the material can be determined from the second law of thermodynamics [37]:

$$Tds = dE + PdV, \tag{2.4}$$

where T is temperature, s is entropy, E is internal energy, P is stress, and V is volume. This path will fall closely under the hugoniot, and for simplicity it is assumed that the release path follows the hugoniot. The isentropic assumption comes from assuming that the entropy generated is small in regards to release, since much of the entropy generation occurs during the initial shock loading. Furthermore, the specific kinetic energy and specific internal energy are shown in figure 2.6, where the Rayleigh line bounds the specific kinetic energy and the specific internal energy is the entire area under the Hugoniot.

In order to completely describe the Rankine Hugoniot Jump system, one additional equation is needed; an equation of state is typically the additional equation needed to fully define the shock event. Due to its simplistic nature, a commonly used equation of state for solids in shock physics is the Mie Grüneisen equation of state (EOS) [39]:

$$P = P_H + \frac{\gamma_o}{V}(E - E_H), \tag{2.5}$$

where, P_H and E_H are the pressure and specific internal energy at the Hugoniot state, and γ_o is the Grüneisen parameter. The parameter is a ratio of vibrational frequencies of atoms in a lattice to the change in volume. As a material is shocked, the electrons of the atoms begin to oscillate at higher and higher frequencies, which is directly associated with a change in volume. This in turn is the reason that the Mie Grüneisen EOS works well for materials not exhibiting phase changes during shock. This EOS only applies to regions of compressive stress and strain where elastic-plastic deformation is occurring.

Another equation of state utilized in simulations to characterize complicated materials, such as water, is the Analytical Equations of State (ANEOS) software created by Samuel L. Thompson at Sandia National Laboratory in 1990 [40]. These values are analytically calculated using thermodynamics to accurately model the solid, liquid, vapor, and plasma phase of a material of interest. This type of EOS works well for water, which is one type of material that experiences phase transitions during a shock event, such as from water to steam. This EOS will be used in conjunction with the Mie Grüneisen EOS to model both water saturated and ice sand mixtures.

With the conservation equations and the equations of state defined, a process known as impedance matching can be explained. Each material involved in a planar shock wave experiment possesses different impedance, defined by *Z*, which is related to density and sound speed. The following equation presents this relationship [30]:

$$Z = \rho_o U_s \,, \tag{2.6}$$

where, ρ_o is the initial density and U_s is the shock velocity. When these materials interact with one another, impedance matching allows the Hugoniot to be determined. In simulations, the Hugoniot states for particle and shock velocities as well as stress, can be taken directly from tracer information within the material. However, in an experiment, impedance matching helps to obtain information where data acquisition is not available, which helps to characterize the material of interest. For example, in planar shock experiments with sand, data acquisition devices cannot be placed directly in the sand, but by taking information from manganin gages or PDV measurements, data can be backed out from impedance matching methods by algebraically determining the sand's particle velocity and shock velocity at the Hugoniot state.

All that is needed for impedance matching is the initial density, sound speed, and Hugoniot slope to characterize a given material. Typically impedance matching occurs with materials that have been well characterized by planar shock impact experiments, such as copper, iron, and steel in conjunction with a material of unknown shock properties, in order to obtain density, sound speed, and slope of the Hugoniot for the material of interest [41]. Figure 2.7 presents an example of an iron Hugoniot with each data point representing a different impact speed. This assumes that an Iron flyer is hitting an iron target, where the recorded particle velocities are one-half the impact speed; this is characteristic of identical homogenous materials and furthermore a characteristic of identical impedances.

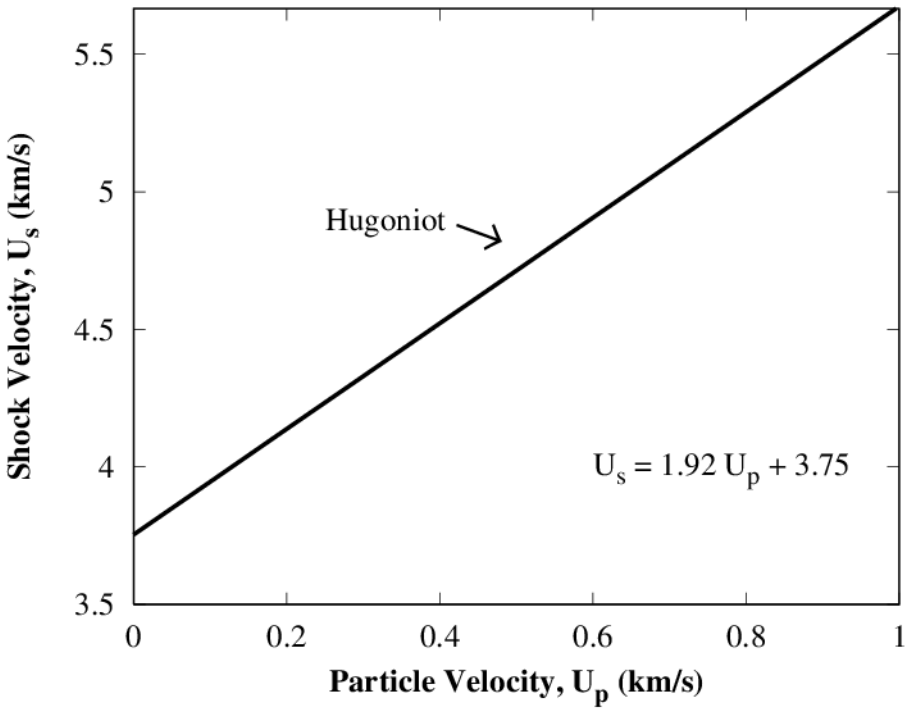

Figure 2.7 Us-Up Space for an Iron Hugoniot, with shot speeds from left to right of 100, 500, 800, 1200, and 1600 mps

The representation of the Hugoniot in Us-Up space is different from figure 2.6, which is in P-v space, however both of these plots convey the same information. The equation in figure 2.7 relates the shock velocity to the particle velocity with the general equation stated as follows:

$$U_s = sU_p + C_o\,, \tag{2.7}$$

where, U_s is shock velocity, U_p is particle velocity, s is the Hugoniot slope, and C_o is the extrapolation of the line fit to zero stress, which is the approximate sound speed of the material. So for the iron equation above, the slope of the Hugoniot is 1.92 and the sound

speed is generally around 3.75 km/s. These values are the reference values used for impedance matching. Equation 2.6 can be related to equation 2.4 by algebraically combining the conservation equations, 2.1-2.3 with equations 2.6 and 2.4. Assuming the Rankine-Hugoniot jump conditions, these equations can be related for different variables depending on what is given and what needs to be calculated. A list of these algebraic relationships can be found in Meyer's *Dynamic Behavior of Materials* on pg. 116 [39]. The following utilizes equation 13 from Meyer's table:

$$P = \rho_o(C_o U_p + s U_p^2) , \tag{2.8}$$

where, ρ_o, C_o, s are the initial density, zero stress sound speed, and Hugoniot slope respectively of the given material of interest.

Now that the equations have been derived, lets do an example. Assume that a copper flyer traveling at 800 meters per second (mps), with a density of 8.930 g/cm^3 ($\rho_{o,Cu}$), a zero stress sound speed of 3.94 kilometers per second ($C_{o,Cu}$), and a Hugoniot slope (s_{Cu}) of 1.489, impacts iron with a density of 7.850 g/cm^3 ($\rho_{o,Fe}$), a zero stress sound speed of 3.574 kilometers per second ($C_{o,Fe}$), and a Hugoniot slope of 1.920 (s_{Fe}) [37]. Determine the Hugoniot state reached in the iron for particle velocity and stress.

Copper and Iron were used in this example as both have been well characterized in planar shock experiments. With these values and equation 2.8, figure 2.8 presents these results as a relationship between stress and particle velocity for a range of shock velocities.

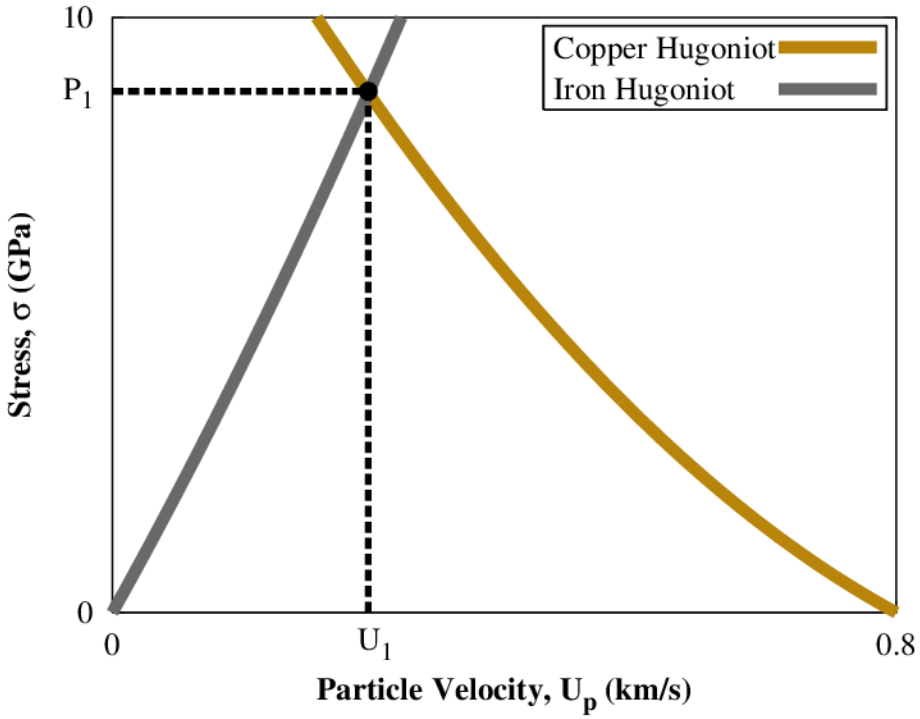

Figure 2.8 Shock Interaction Between Copper and Iron

The intersection of the two lines represents the Hugoniot state of the particle velocity and the stress; this intersection also corresponds to where the respective Rayleigh lines would intersect. The value at the intersection is important in determining information from experiments where measurement devices for velocity could not be present at this interface. In experiments, the only data acquisition device that could be present would be a pressure gage, but from this pressure a particle velocity can be calculated.

Additionally, impedance matching gives a rough insight into what typical values should be expected in an experiment and helps to setup future experiments in which certain data is to be obtained for given impact velocities. As a reminder, impact velocity

should not be confused with particle velocity, as the impact velocity is the speed at which the projectile is traveling before impact.

Impedance matching can also provide information of the release states on the free surface of the material of interest by taking the first Hugoniot state and substituting these new values into equation 2.8. By calculating the impedance (Z) of each material with equation 2.6, it can be determined if and how the material releases. Since iron has lower impedance than copper, the copper flyer iron will release until it approaches the impact velocity of 800 mps. It should be understood that the release states will not fall on the Hugoniot of the material, but will instead follow the isentropic release path that is calculated by equation 2.4. However, since the hugoniot and the isentrope are so close together, it is assumed the release follows the Hugoniot to equilibrium.

By flipping the Hugoniot of the iron for each state of release and re-shock, each state can be determined. This is shown in figure 2.9 below, which presents release states at different particle velocities.

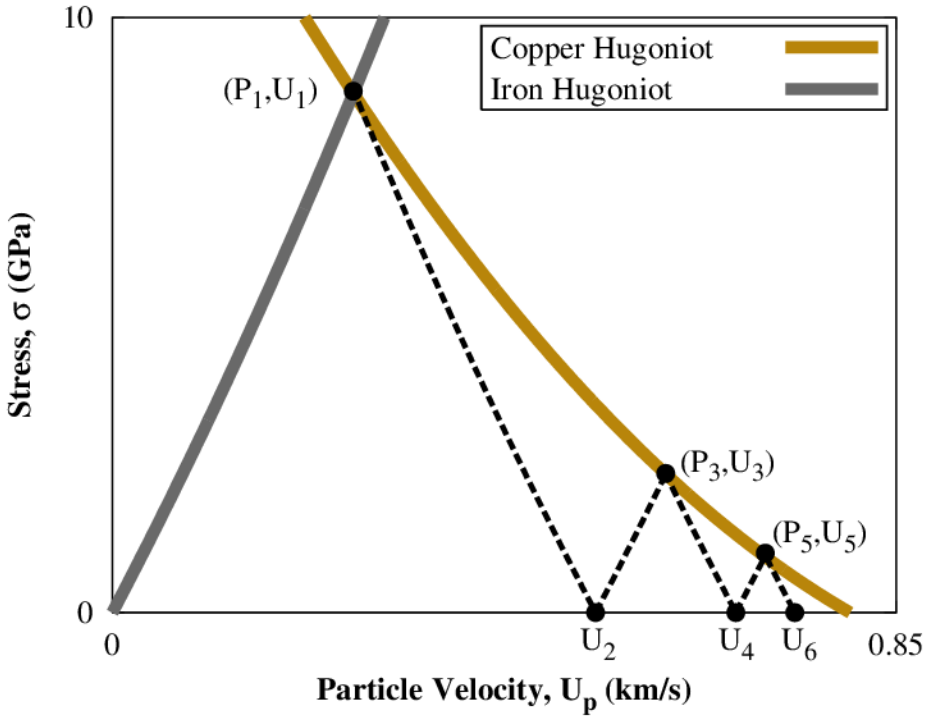

Figure 2.9 Release of Iron from a Copper Flyer Impact

Since the back surface of the Iron is a free surface, the pressure of propagating shock waves is allowed to release and the iron expands. This release is seen in states U_2, U_4, and U_6, which correspond to the points at which iron's Hugoniot equation cross the x-axis at zero pressure. U_3 and U_5 correspond to re-shock states in the iron as the shock waves reverberate between the copper / iron interface and the iron free surface. These shock waves will reverberate until all of the induced pressure is released and the particle velocity of the iron approaches the impact velocity of the copper. These release states give insight into how the energy is stored and released during a shock event and this information becomes important in analyzing heterogeneous materials beyond just its mechanical properties.

2.2 Shockwave Dynamics of Heterogeneous Materials

The proceeding sections have only considered homogeneous materials, meaning that materials are composed of one material and are assumed to have little to no porosity. The materials of interests in the experiments are heterogeneous materials, meaning the materials are composed of two or more constituents and contain porosity, or void between materials. Dry sand is a heterogeneous material since it is porous and does consist of air gaps between sand grains. Water saturated sand and ice sand mixtures consist of three material components: sand grains, water/ice molecules, and pores or void space.

Heterogeneous materials act differently under shock loading as compared to homogeneous materials. As a shock wave passes through a heterogeneous material, pores are crushed and the porosity is reduced towards that of its homogenous constituents. This results in the bulk density or specific volume of the material changing rapidly in comparison to the shock stress. Figure 2.10 depicts the rapid change of density in sand for a given stress loading as compared to its homogeneous constituent, solid quartz.

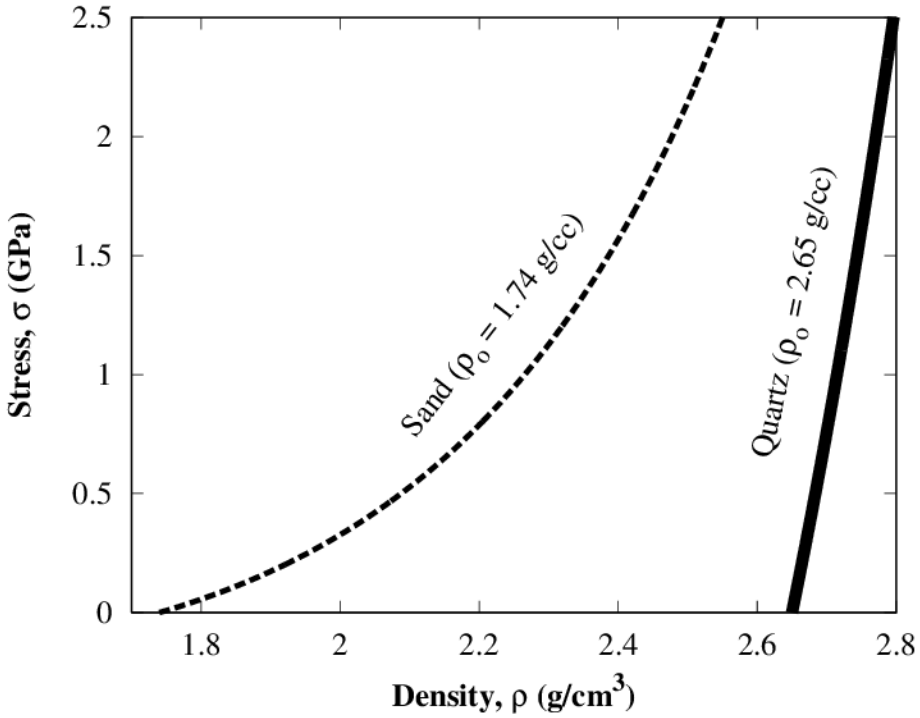

Figure 2.10 Comparison of Quartz and Sand Hugoniots

At higher impact velocities, the material behaves more like a homogenous material once the porosity is crushed out. The Hugoniot of the sand will never quite reach the solid quartz Hugoniot, due to irreversibility from entropy generation. Although it is not shown in figure 2.10, once the sand Hugoniot approaches the quartz Hugoniot, the Hugoniot will start to curve up and around, as the entropy generation increases. As was mentioned in the introduction, since the experiments are reaching stresses of values between 1 and 4 GPa, there is no phase transition of the quartz and complete crushing of the porosity is never quite reached. Complete crushing of porosity and phase transitions for most quartz-based sands occurs between a flyer impact speed of 1200 and 1300

meters per second [25], whereas most of the experiments simulated in this document fall less than 1000 meters per second. This phase of quartz is known as stishovite [25].

The difference between homogeneous and heterogeneous materials can further be seen from a stress-strain relationship. This is known as the Swegle-Grady stress strain power law curve, as shown below in figure 2.11 [42]

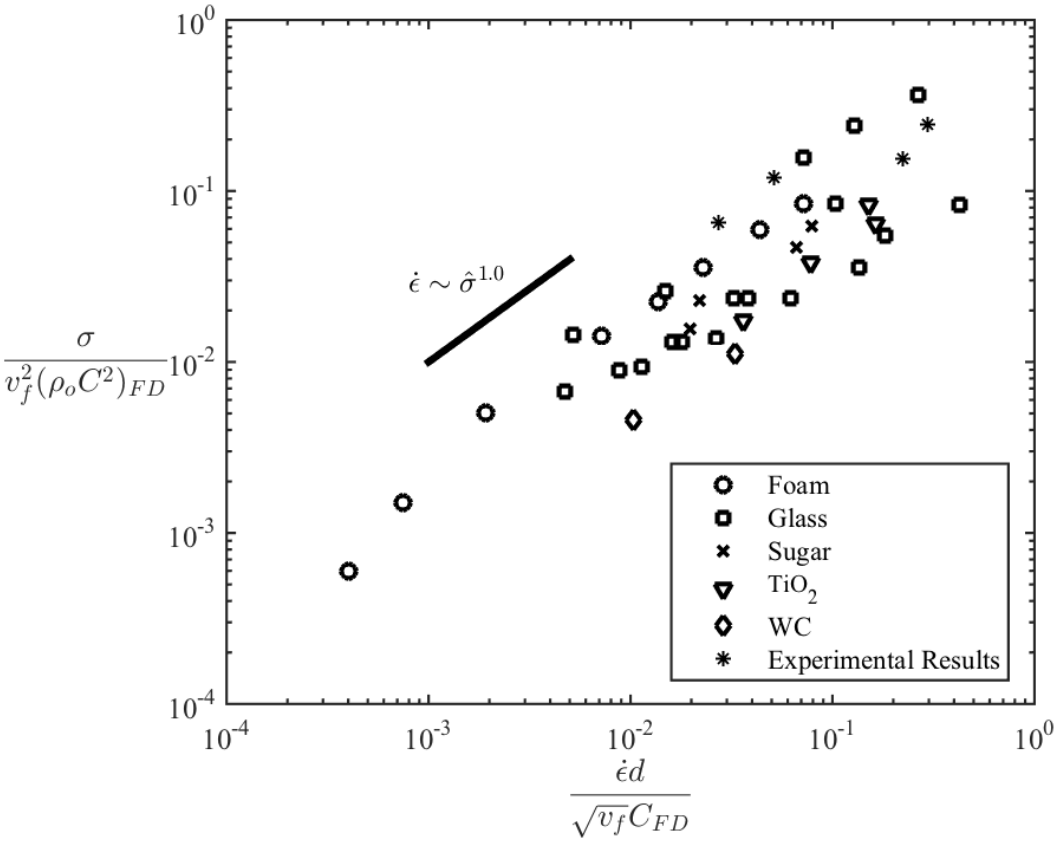

Figure 2.11 Swegle – Grady Stress Strain Power Law Relationship for Brittle Heterogeneous Materials

The y and x-axis are non-dimensional versions of stress and strain rate, respectively. This allows for the materials at different impact speeds (v_f), particle

diameters (d), sound speeds (C), and densities (ρ) to be normalized to give the stress and strain rate relationship found in heterogeneous granular materials. The experimental results are for the Georgia Tech Dry Sand experiment that is in this document. Notice for heterogeneous materials, strain power is related proportionally to stress to the first power. In the same paper from which figure 2.11 is derived from, it suggests that strain power for homogenous materials plotted in a similar fashion is related proportionally to stress to the fourth power, also known as the "fourth power law" [18]. This useful relationship will be utilized in validating both experiments as well as simulations in ensuring that the material of interest behaves like a heterogeneous material when subjected to shock loading. Furthermore, this method of characterization of materials will be used for water saturated and ice sand mixtures.

2.3 Experimental Data Acquisition

It is essential to have a basic understanding of how data is extracted from planar shock experiments before simulations and models can be validated. In this document, only three data acquisition methods will be explained, as these three methods are the most widely used in the field; these three methods are: 1. Manganin and Polyvinylidene Fluoride stress gages (PVDF), which measure voltage and then converted to give stress in GPa, 2. Velocity Interferometer System for Any Reflector (VISAR), which takes frequencies produced from a surface velocity and eventually converts this voltage reading into a particle velocity [43], and 3. Photon Doppler Velocimetry (PDV), similar to

VISAR, utilizes displacement instead of velocity from light reflections off of a free surface to determine a beat frequency and eventually convert to a particle velocity [43].

The gages mentioned, manganin and PVDF, work differently, but obtain similar results. Manganin gages are one of the oldest types of measurement devices in the shock physics community, along with make and break pins [37], however with the new methods, such as PVDF, PDV and VIASR, these types of measurement are beginning to fade away. Manganin gages typically 1-3 mm in width and are used to measure stresses in materials to help determine Hugoniot state values. Shown on the left in figure 2.12, taken at Marquette University, is an example of a Vishay manganin stress gage, encapsulated in Mylar and epoxy on a sheet of aluminum to help protect the gage during the shock event, before it is destroyed as shown on the right.

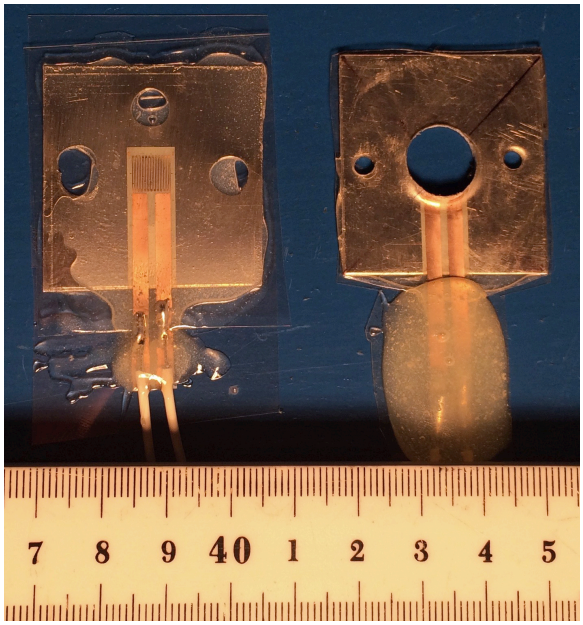

Figure 2.12 Manganin Gages Before and After Impact

Manganin is a copper-manganese nickel alloy that has a high sensitivity to hydrostatic pressure and the change in electrical resistance, as a function of stress, is linear to extremely high stresses [44]. Also, manganin is only sensitive to a change in stress and not in temperature, which is perfect for regimes of stress induced by dynamic shock loading. Therefore, when a voltage is applied across the gage, any induced stress on the gage will result in a change of resistance and subsequently a change in voltage, which can be measured with an oscilloscope. These gages are not as reliable as other acquisition methods and have proven to be an outdated resource due to more accurate and robust methods for measuring particle velocity. Additionally, each gage is assumed to follow the same calibration curve, since it would impossible to calibrate each gage, as the gages plastically deform with increased stress and are relatively expensive. The calibration curves are either from Sandia National Laboratory or Israeli line fits to obtain the correct stress results [45].

PDVF gages are similar to Manganin gages, however the voltage output is caused from a piezoelectric response when compressing the PVDF during shock loading. This voltage response is then converted to a stress measurement to allow for stress history data. This stress history data, combined with impedance matching, can be used to calculate the Hugoniot state. The reliability of PVDF gages are quite poor and actually provide information that looks “smoothed” rather than a “jagged” typical stress data that is obtained from manganin gages. This is due to the output voltage from PVDF being based on an accumulation of charge and therefore the stress response is not an immediately recorded process.

Additionally, PVDF gages cover a much wider area than a manganin gage, and provide response information that looks similar to a homogenous material due to spatial averaging. Nonetheless, both of these gages have proved to be reliable and accurate for calculating time of arrival of a projectile, which prove useful for gas and powder guns that might not possess methods of accomplishing this feat.

Another method, and perhaps the second oldest of the data acquisition devices is Velocity Interferometer System for Any Reflector (VISAR), which was first developed in the 1970s by Sandia National Laboratories [43]. This type of device measures particle velocities on the back free surface of the material opposite the flyer side of the material. Typically, there are windows that contain and push the material flush against the driver; these windows are sputter-coated with microns thick copper, gold, or silver to allow for the laser light to reflect off a surface, hence the reflector name in VISAR. When this reflective surface moves during a shock event, the VISAR interferometer produces light fringes proportional to a specimen's surface velocity [43]. This differs from PDV, as will be discussed, since PDV utilizes the material surface's displacement rather than velocity.

Similar to VISAR, Photon Doppler Velocimetry (PDV) uses an infrared laser light at 1550 nm that utilizes reflections from the surface of interest (often covered in a reflective coating) which produces light fringes directly proportional to displacement [43]. PDV systems can be classified into one of two types: homodyne and heterodyne. Homodyne systems use one laser power source for both a reference and a target. The difference in the unaltered reference light and the reflected light collected from the target (shifted due to its motion) produces a beat frequency, which is converted from a light intensity to a voltage measurement. Finally, via a Fast Fourier Transform (FFT)

algorithm, the voltage can be related to the particle velocity. Heterodyne systems are more robust by utilizing two different lasers, one for the target and another for the reference. As the beat frequency is derived from the difference between the target and reference light, using a heterodyne system allows the reference lasers to have a greater contrast to the target light increasing resolution of fringes. Figure 2.13 shows the newly developed homodyne PDV system at Marquette University that is currently in operation.

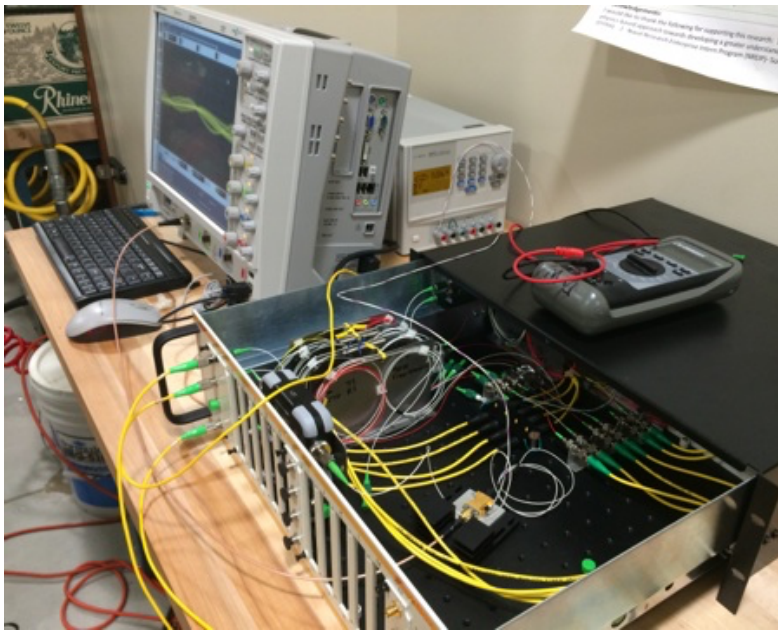

Figure 2.13 Marquette University Homodyne PDV Measurement Device

As of now, this setup only utilizes one channel, or in other words can only measure one point of the surface. The Marquette PDV will be modified to include more channels to measure more points of response on a given sample, while still remaining homodyne.

There are software packages developed by Sandia National Laboratories and other labs in Academia that convert voltage signals from PDV using an FFT scheme to calculate the velocity from the beat frequency. For both VISAR and PDV, the proportionality of the beat frequencies to the given type of measurement is different, PDV utilizing displacement and VISAR utilizing velocity, and the ways of extracting the information vary from method to method [43].

III. COMPUTATIONAL SETUP

3.1 Mesoscale Simulations

Mesoscale is a scale between micro and macro, and allows for unraveling of information by observing the interactions of different particles in a heterogeneous material. The conventional way of setting up shock simulations treats the material as a bulk homogeneous medium, with assigned bulk properties, such as utilizing a p-alpha or p-lambda model as will be described below. Instead of observing grains and how each individual particle behaves under compaction, unlike in a Mesoscale setup, the bulk material model is not concerned with these factors. Bulk simulations are nice for preliminary setting up an experiment with both one-dimensional and two-dimensional geometries; however, if more precise information is to be extracted and better models developed, Mesoscale simulations prove to be a more accurate choice when simulating.

As mentioned above a bulk method that is commonly used to apply a constitutive model, known as the p-alpha model, to an equation of state. Models such as the p-alpha have parameters associated with porosity and help modify bulk equations of state in order to represent heterogeneous materials. The following presents the p-alpha equation of state [29]:

$$P(\rho,T)=\frac{1}{\alpha}P_s(\alpha\rho,T)=\frac{1}{\alpha}P_s\left(\rho_{s,}T\right), \tag{3.1}$$

where the distention parameter, α, relates the porous density of a heterogeneous material to the density and pressure of a solid homogeneous material (no voids), ρ_s and P_s respectively. The distention parameter has been defined for various materials and other analytical models for alpha have been developed to better represent ductile porous materials like iron or copper [19].

The p-alpha equation of state assumes an elastic and a plastic regime bound by a theoretically bulk Hugoniot. This particular model can be used in larger simulations for industrial processes where resolving each grain in a process, like a Mesoscale simulation, would be too computationally expensive [23].

A good example of this model is presented for the Marquette Brake Pad powder dynamic compaction tests in figure 3.1. The data shows static compaction results in comparison to dynamic shock compaction for the Brake Pad powder. It can be observed that the p-alpha model contains both the elastic and plastic bounds for the brake pad powder.

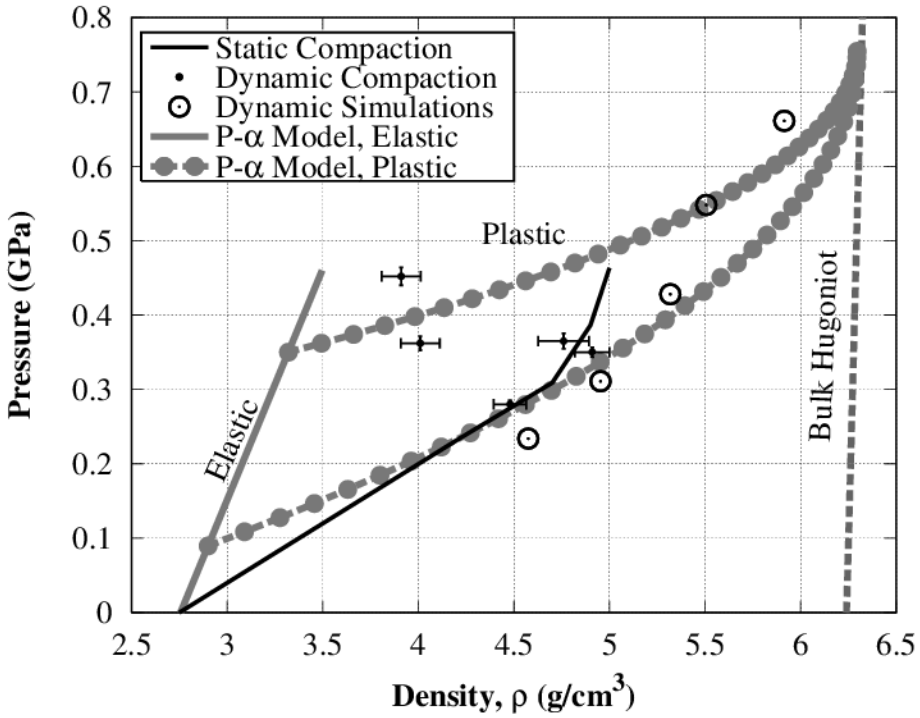

Figure 3.1 P-alpha Model for the Dynamic Compaction for a Brake Pad Powder

Although the data does not match the simulations well for lower velocity shots, it does approach the bulk Hugoniot as would be expected for subsequently higher impact velocities. It is apparent that mesoscale simulations provide a better overall understanding of grain interactions and as will be discussed for the Marquette dynamic compaction of the brake pad powder and for the water and ice sand mixtures, these interactions between the grains can help to give a picture of what stress and temperatures are involved at those grain surfaces.

3.2 Mesoscale Simplification Setup

Setting up the mesoscale simulation in CTH involves a greater amount of steps than a bulk simulation in order to ensure a complete and correct model. The first step is to setup the geometry of the grains. For dry sand experiments, this geometry can be simplified to consist of mono-dispersed spheres, meaning all of the particles are the same size in diameter, and setup in a random orientation, which is related to the apparent density of the granular material. Water-saturated sand and ice sand mixtures will be discussed below. Also to be discussed in the *Sensitivity* Analysis section, spheres are assumed to be the most accurate geometry depiction for sand, as these types of simulations with this geometry match well with planar shock experiments of brittle granular materials [33].

This random orientation ensures a material will behave in a manner similar to heterogeneous materials, since real-life sand geometries arrange in a random orientation. A more structured orientation of the grains, such as cubic closed pack or hexagonal closed pack (hcp) produces geometries that are not similar to what is actually observed in images of sand. Figure 3.2 below shows an experimental image on the left taken at Georgia Tech of Oklahoma sand (Courtesy of Dr. Naresh Thadhani and Dr. Gregory Kennedy of Georgia Tech) and the image on the right is a two-dimensional slice from a Fortran code Mesogrow, written by Dr. John Borg that places mono-dispersed spheres in a random orientation.

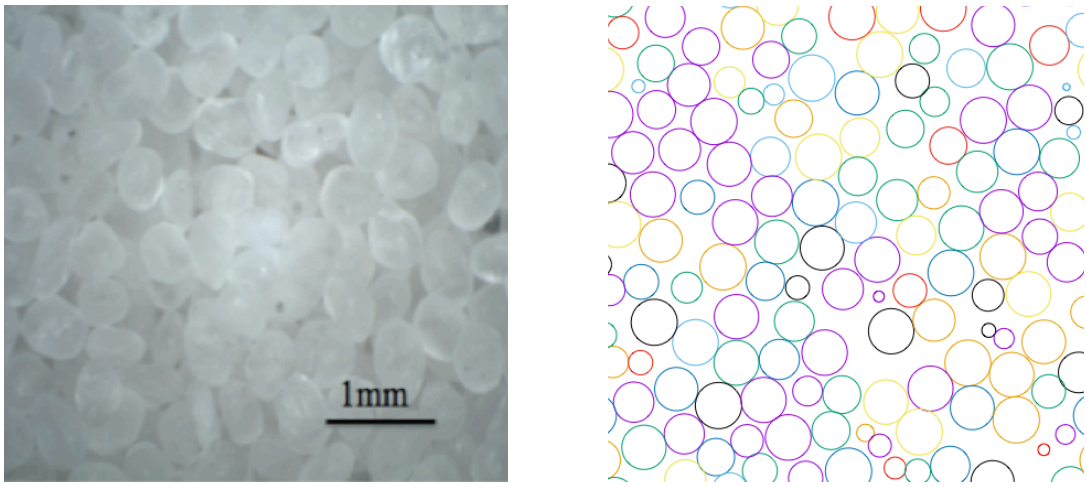

a) Oklahoma Sand, 450 μm **b)** Slice of the Computational Domain

Figure 3.2 Comparison of Oklahoma Sand in Experiments and the Computational Domain

The Oklahoma sand shown on the left is approximately 450 microns in diameter. The circles shown on the right in the two-dimensional slice of the computational domain are not all the same size since some of the grains out of the plane, have conic sections that are shown. The different colors represent the different material number specification so that when the created geometry is inserted into CTH, it works with a command known as "SLIDE" which models the slipping of grains, as seen in experiments. This will be discussed in more detail in section 3.4 *Modeling Strength, Fracture, and Stiction*.

The Mesogrow code developed by Dr. John Borg at Marquette University randomly generates a set of points and grows grains at those points to a specified diameter and volume fraction. However, spheres packed randomly cannot occupy space very efficiently and can only reach volume fractions of about 60% [46]. Some of the sand used in these experiments has volume fractions of 65 % to 70%. FCC packing can reach volume fractions of 74% [46], however as was mentioned earlier, this type of geometry

produces results much more similar to homogenous materials than heterogeneous materials. In order to get volume fractions higher than 60% while still keeping the random orientation of the spheres, a "shake and pack" method is utilized in Meso-Grow.

"Shake and pack" takes the positions of the spheres and "shakes" the domain by shifting the position randomly while ensuring no overlap occurs. Once this "shake" operation has been completed, more spheres are "packed" into the spaces that have not been occupied by grown grains. This method can produce volume fractions of up to 68%. If 70 % were the volume fraction of the sand in the experiment, using 68% for the volume fraction of sand would have a huge affect on the results, as was noticed in the section *Sensitivity Analysis* for varying the volume fraction. By allowing a little overlap for all grains, or in other words slight indentation of the grains, a higher specified volume fraction can be obtained; for fine powder that are statically compacted before a planar shock experiment, this overlap helps to model deformation and indentions into other grains when packing a box of sand to a high volume fraction.

Another method to incorporate overlap is to utilize another code known as LAMMPS, a molecular dynamic simulation code developed by Sandia National Laboratory. Although the software is utilized for looking at atom on atom interactions, the way grains are placed and grown are similar to Mesogrow. However, LAMMPS also includes coefficient of restitution and friction, and mechanical properties such as young's modulus and Poisson's ratio. These constants can be adjusted to allow for slight overlap or indentations when the grains are grown to a specified volume fraction. LAMMPS also has other methods for setting up sand geometries such as pouring sand grains in a box or

dropping a cube of particles. These methods were shied away from, as specified experimental packing densities were hard to match.

Because of the additional properties and overlap with the LAMMPS grow option, the specified grain radius in LAMMPS was subject to change with the change of mechanical properties and coefficients [47]. As will be seen in Chapter 5 for the Cambridge case study, the grains were grown to the wrong size of 244 microns instead of 190 microns, but kept at the same volume fraction. Although this allowed for an interesting find in the dynamic bulk response of the builder's sand by varying the grain size, it did not grow the grains to the average bulk size of 190 microns. More research is needed in understanding how LAMMPS could utilize overlap while keeping the grains to the right specified size.

More complicated geometries can be incorporated with poly-dispersed spheres, meaning the size of the grains is associated with a distribution of diameters, as seen in real life sand. Not only would this be more characteristic of sand, it would allow for a higher packing density. However, due to the Eulerian nature of the hydrocodes, resolving the smaller grains in the computational domain increases the total number of cells, and therefore increases the amount of computational time needed to ensure mesh convergence.

3.3 CTH and iSALE Setup

After the geometry of the sand grains have been setup to a specified size and volume fraction, this geometry is then inserted by writing the locations of the spheres to a CTH input script. Before talking about the input script, CTH has a solution sequence that needs to be discussed prior to inputting mesoscale geometries.

CTH utilizes a Eulerian-Lagrangian solution sequence in order to simulate a planar impact experiment. Eulerian codes treat a continuum variable, such as temperature or stress, from a fixed frame of reference, where the conservation and motion equations are solved using a fixed mesh fixed in space. This means that the material moves through the mesh. Lagrangian codes treat a continuum variable from a frame of reference fixed to the material, where the conservation and motion equations are solved using a frame fixed to the material where the mesh moves through space, or the mesh moves with the material [29]. The conservation equations, 2.1, 2.2, and 2.3 are slightly altered in order to work in collaboration with CTH. The following altered conservation equations, also known as the Von-Neumann equations are as follows [29, 31]:

Mass:
$$\frac{\partial \rho}{\partial t} = -\rho \vec{\nabla} \cdot \vec{V}, \tag{3.2}$$

Momentum:
$$\rho \frac{\partial \vec{V}}{\partial t} = -\vec{\nabla} P - \vec{\nabla} \cdot \left[\sigma + Q(\vec{V}, c_s) \right], \tag{3.3}$$

Energy:
$$\rho \frac{\partial E}{\partial t} = -P \vec{\nabla} \cdot \vec{V} - \left[\sigma + Q\left(\vec{V}, c_s\right) \right] \cdot \vec{V}. \tag{3.4}$$

The above equations are in differential due to easier formulation for computational stepping schemes, and possess two new terms: σ and Q. The σ is associated with the stress tensor and Q is an artificial viscosity term. Without the artificial viscosity term, the discontinuities associated during a jump from a reference state to a shocked stated would dominate the computation, causing convergence issues between cell to cell [31]. The artificial viscosity allows for a "smoothing" of the jump between the states by presenting the code with linear and quadratic representations. Artificial viscosity is also related to the strain rate in the direction of material acceleration [31]. This gives more accurate and realistic shock profiles that are found in experiments.

The time step is calculated from the Courant Stability Theorem, which is shown from the following approximated equation [29]:

$$\Delta t < f_{safety} \min\left(\frac{\Delta x}{|v_x| + c_s}, \frac{\Delta y}{|v_y| + c_s}, \frac{\Delta z}{|v_z| + c_s}\right), \tag{3.5}$$

where, f_{safety} is a safety factor equal to approximately 0.6 , Δx , Δy , Δz is the minimum grid spacing in each direction, $v_{x,y,z}$ is the local particle velocity of the material in a particular cell, and c_s is the local bulk sound speed of the materials in the cell.

For mesoscale simulations of heterogeneous granular materials, the given grid spacing is calculated directly from the size of the grains. 10-11 computational cells across each sand grain in both the lateral and longitudinal directions have proven to be enough to ensure mesh convergence for heterogeneous granular materials [33]. The grid

spacing, or cell size, defines the overall amount of cells for the entire computational domain and dictates how long the simulation will run.

It should be noted that simulations are never fully resolved at the beginning of setting up an experiment and the simplest model is assumed. The "simplest model" means that fracture, yield strength, and other options like slide, which will be discussed later on in the document, are not included. Also, 5-6 cells across each grain are utilized; these results are compared to experimental data to look for slight validation. It is not until after this simplest model that a fully resolved simulation should be run. Other reasons would include testing the geometry that was built with Mesogrow and sparing the user from making simple mistakes.

For each time step in CTH, a sequence of solutions occurs, which is presented in table 3.1[29].

Table 3.1 CTH Solution Sequence

Step Number	Name of Step	Reason for Step
1.	Lagrangian Step	Lagrangian forms of the conservation and motion equations are solved
2.	Remap Step	The distorted mesh from the Lagrangian step is fixed onto the original mesh, which is Eulerian in nature
3.	Database Modification Step	The overall input is changed according to user options such as discarding not needed materials, adding a velocity to a material for a given time step, and various other options
4.	Time Step Calculation	Based on equation 3.1.

The speed at which these solution steps occurs is not only dependent upon the time step, but also varies with the parallelization of the code, or running the simulation on multiple central processing unit (CPUs) in order to "speed" up the calculations.

Garnet, which is the supercomputer utilized for these simulations, is operated by the United States Department of Defense's Engineer and Research and Development Center Supercomputing Resource Center (ERDC DSRC). When running simulations on Garnet, asking for a certain number of nodes when launching a simulation specifies the amount of parallelization that is needed. A node is defined as a rack or set of CPUs, which on Garnet contains 32 CPUs in which the calculations may be performed [32]. Optimizing the number of nodes to ask for is one by allocating roughly 10,000 to 50,000 cells from the mesh to a single CPU [29]. For example, if there are a total of 50 million

cells, which is average for a three-dimensional planar shock model, and 50,000 processes are specified per CPU, a total of 1000 CPUs are needed. In order to determine the number of nodes needed to meet the optimization criteria, the 1000 CPU value is divided by 32, since there are 32 CPUs per node. This gives a total value of approximately 32 nodes to ensure that 50,000 processes per CPU occur.

Another important factor in ensuring stability of the code and to correctly model a planar shock experiment is to impose proper boundary conditions for all boundaries in the x,y, and z direction. CTH offers a range of selections for boundary conditions, which are described in table 3.2 below [29].

Table 3.2 Boundary Conditions Offered by CTH

CTH Specification	Type	Explanation
Symmetry Boundary Condition	0	Boundary velocity is set to zero, and is used to typically simulate a reflecting boundary condition.
Sound Speed-Based Absorbing Condition	1	The mass may flow in and out of mesh, simulating an infinite or semi-infinite medium.
Outflow Boundary Condition	2	Mass may leave the mesh. This can be used to simulate a free surface.
Inflow Boundary Condition	3	Mass may enter the mesh.
Outflow/extrapolated pressure boundary condition	4	Mass can leave the mesh while maintaining a constant pressure, which can be utilized to simulate an atmosphere for example.
Symmetry Boundary Condition with Void Inflow	5	Like type 0, except void can flow into the domain.
Periodic Boundary Condition	6	Material flows to the opposite boundary, which is utilized to treat infinite or semi-infinite materials.

The two boundary conditions utilized for most of the planar shock experiments are Type 1: Sound Speed-Based Absorbing Condition to simulate the flyer and window in the direction of shock, and Type 6: Periodic Boundary Conditions to simulate the boundary for material of interest in the non-axial directions. Type 4 boundary conditions are used sometimes to lessen the amount of cells used for the computational domain. In order to use the periodic boundary condition, it has to be assumed the material is a somewhat infinite medium, as is true for these mesoscale simulations; the material

domain is on the scale of millimeters, where the experimental target is on a scale of centimeters.

The periodic boundary conditions that are instated in the axial directions allow the material to flow out one side and to continue flowing to the other side symmetrically. The Mesogrow code, mentioned earlier, builds the grains so that if the grains are grown at the edge of the boundary, that part of the grain that exits the domain grows on the opposite side of the domain to ensure the periodicity of the material.

3.4 Modeling Strength, Fracture, and Stiction

The last important aspect of setting up CTH involves the mechanical properties of the material of interest. Yield strength of materials, which is normally thought of in mechanical engineering for solids to be the point where a material would not return to its original shape when loaded to the elastic limit. This yield strength is similar in shock physics, however it is known as the dynamic yield strength, or the Hugoniot elastic limit (HEL). The HEL can be observed on shock wave profiles for homogenous materials, where there is a slight plateau before reaching a Hugoniot state; this is where the material goes from an elastic-plastic regime to a plastic regime, and an elastic wave, possessing a greater sound speed, breaks out ahead of the plastic wave.

There are a few strength models used to model the mechanical behavior of materials before reaching the HEL. The two models used in this study were Von Mises and a Johnson Cook strength models. The Von-Mises strength model was used for quartz and other materials in the brake-pad powder, due to not having a changing strength in

relation to an increase in temperature. Unlike the Von-Mises, The Johnson Cook strength models were used for materials that had a change in yield strength with an increase in temperature.

In CTH, the Von Mises strength model is known as a linear elastic, perfectly plastic Von-Mises (EPPVM) strength model where the dynamic yield strength, Poisson's ratio, and the melt temperature of the material are the parameters for the option [29]. These parameters must be specified for each type of material, and the yield strength must be the dynamic yield strength, as this is the HEL that is given in literature. Quartz with a density of 2.65 g/cc for example has average dynamic yield strength of 4.1 GPa and a Poisson's ratio of approximately 0.18 [13].

The Johnson-Cook model in CTH has values associated with the equation that relates the yield strength to a change in temperature, which in turn changes the yield "surface". These values can be called out by CTH for a specific material, such as copper. The Johnson Cook model is specifically relevant for ductile materials, due to the changing of the yield strength at higher temperatures, and therefore higher amounts of stresses. This strength model was utilized for the Marquette compaction of a brake-pad powder, since the powder consisted of ductile materials.

An important distinction to make about hydrocodes is their treatment of fracture and friction, because it isn't modeled in the traditional sense like finite element codes or peridynamic codes. In order to model these, new approximations from current options in CTH are utilized. For fracture, a maximum value of strength is set, which is typically either the ultimate tensile strength or about 10% higher than the value found in equation 3.6 [29]. Cells where material exceeds this fracture strength are given void space to

signify the breaking apart of the material. This process alleviates tension as if failure has occurred in a material. These tensile values are specified as negative since compressive stresses in CTH are positive values.

Friction cannot be truly modeled in CTH, but can be approximated with an option known as the "SLIDE" option. Without the slide options, materials "weld" or create "stiction" when particles come into contact with their neighbors, because materials with the same material number cannot be torn apart when they are both in the same cell, which is not necessarily true of a heterogeneous materials under planar shock. Since the friction of sand grains amongst one another is low during the initial onset of a shock wave propagating in the material, the material slides with one another allowing for the response to be more granular in nature. The "SLIDE" command sets the shearing velocity gradients to zero in mixed cells containing two different materials.

In order to make grains with similar properties, these materials are given different material numbers, but still possess the same properties. This way, when a cell has a mixed amount of two grains, the code can tell them apart and allow them to slide against one another. Although this is not friction, as friction in these types of codes needs a resolved surface, normal forces acting between the grains, and an associated roughness associated with the material, the results from the simulations with the sliding method prove to be fairly accurate. Figure 3.3 below shows the difference between stiction and sliding.

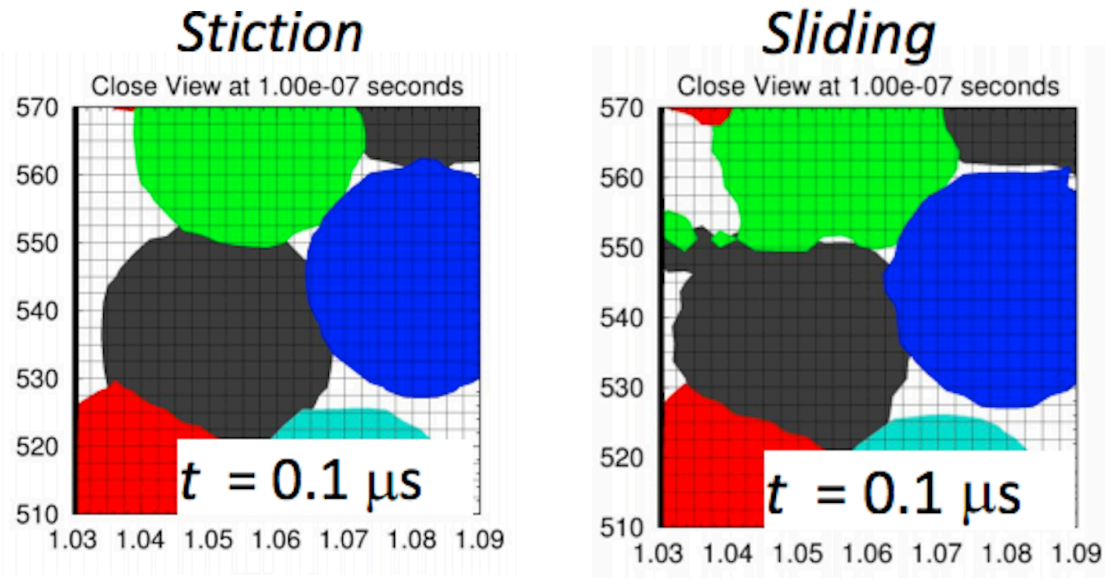

a) Stiction, where the particles weld together once reaching the specified yield strength

b) Sliding, where the shear gradients in all directions go to zero once the material reaches the specified yield strength.

Figure 3.3 Stiction versus Sliding

Notice that the material with the sliding option shows shearing occurring of the material with remnants of the material "floating" in the domain, where the material with stiction shows a homogeneity with the particles "welding" together. The sliding is more indicative of what happens in a planar shock experiment involving sand.

3.5 Sensitivity Analysis

In Borg and Vogler's paper *Aspects of simulating the dynamic compaction of a granular ceramic* [33], an analysis on the input parameters into CTH has been observed. Since iSALE and CTH are similar codes, it will be assumed that the results of this

analysis are consistent. It should be mentioned that the findings in this paper are for two-dimensional setups and do not necessarily correspond to three-dimensional simulations; however, many of the findings are accurate and have been utilized in setting up three-dimensional simulations. Although these experiments are conducted with granular Tungsten Carbide (WC), and the simulation parameters and inputs that most significantly affect the response are also critical in the evaluation of sand.

In the paper, there are discussions on three different studies, each having numerous subcategories, which are as follows:

1. Baseline response
    a. Bulk compaction response
    b. Boundary conditions, domain size and resolution study
2. Parametric study: bulk response as a function of micro-scale variations
    a. Micro-scale Hugoniot: slope and zero stress sound speed
    b. Fracture strength
    c. Elastic properties: dynamic yield strength and Poisson's ratio
3. Parametric study: bulk response as a function of macro-scale variations
    a. Initial volume fraction
    b. Grain morphology
    c. Grain size distribution

Each of these sections delves into the complexities met with setting up simulations in CTH. In this section each of these studies and findings will be discussed, and how these inputs have been modified for the simulations in this document. The main finding in the baseline response is that the computational values for varying impact

speeds produced a Hugoniot that fell under the experimental Hugoniot, suggesting a less stiff material.

3.5.1 Micro-Scale Variations

The boundary conditions that gave the most accurate results were either rigid or period boundary conditions in the lateral directions, since these conditions satisfy the uniaxial strain conditions. The boundary conditions in the shock direction are outflow to allow mass to enter and exit the domain while holding a constant pressure at those boundaries. Outflow boundary conditions in the lateral direction caused a 5% difference in stiffness in the bulk shock response, according to the findings.

The domain size was varied for these simulations from 2 to 5mm in the lateral direction, with no variation in the bulk response. In the direction of shock, it was important that this distance did not change for the validation of the experiments depended on this remaining the same. The lateral size of the domain will change depending on what type of data acquisition is utilized in the experiments, since gages are approximately 3 to 4mm in length and some VISAR spots are 3 mm in width. These findings in Borg's paper allow for lateral domain variation to not affect the bulk dynamic response of the heterogeneous material.

As was discussed earlier in *Chapter III Computational Setup*, the best mesh resolution for convergence of a dynamic bulk response is 10 to 12 cells per grain. Therefore, in order to not utilize more processors than actually needed, 10 cells is utilized

in order to have mesh convergence while maximizing the efficiency of the computer's processors.

Observing the micro-scale Hugoniot properties, such as the slope of the Hugoniot as well as the zero stress sound speed, and varying these by 5 to 10 percent, had little to no affect on the dynamic bulk response. The variation of fracture strength by 5 to 10 percent did not affect the dynamic bulk response either. However, the fracture strength model in CTH does not allow the yield strength to go to zero once these stresses are experienced in a shock event and does not accurately portray grain fracture. A Lagrangian and Eulerian mesh scheme do not adequately resolve fracture and friction. These are important factors in understanding the release of heat. Even with the limitations of an inaccurate fracture model as well as the inexistence of friction, the simulated model cases in this study still closely align with the experimental data.

Perhaps the most important factors in ensuring that experimental validation occurs, is that the elastic properties of the material are properly inserted. Varying the yield strength (Y) by 5-10 percent of the tungsten carbide in the parametric study increased the yield strength increased the stiffness of the bulk Hugoniot, better matching the experimental Hugoniot. Decreasing the yield strength decreases the stiffness of the Hugoniot. The variation in the Poisson's ratio (ν) had similar effects, however this changes the HEL as described by the following equation [37]:

$$\sigma_{HEL} = \frac{1-\nu}{1-2\nu} Y. \tag{3.6}$$

By increasing the Poisson's ratio increases the Hugoniot elastic limit. The limited impact velocities of the experiments in this study ensured that the dynamic response of the tungsten carbide remained under the HEL, such that the variation in Poisson's ratio did not affect the simulated dynamic bulk response.

3.5.2 Macro-Scale Variations

The differences between two-dimensional simulations and three-dimensional simulations come from the variation in macro-scale properties, such as volume fraction, grain morphology, grain size distribution, and particle order. Specifically for grain morphology, the third dimension plays a role in how elastic waves travel through a sand bed with more cells to calculate more accurate volumes for every time step in CTH.

With that said, variations in volume fraction of sand for every experiment can vary by 10 percent, [33]. An increase in volume fraction increases the stiffness of the Hugoniot. It becomes important then when simulating experiments that the volume fraction is matched to experimental data in order to reduce systematic error.

Creating geometries with different two-dimensional shapes, such as circles, triangles and squares, changed the grain morphology. Interestingly, the change in grain morphology of circles and squares did not affect the dynamic bulk response, but the triangular shapes did; reason being is that the triangular geometry causes the material to lock together before shock consolidation, causing the material to behave more like a homogenous material than a heterogeneous material. This "pre-lock" of the triangles results in a stiffer response than the more accurate geometries of circular and square

setups. Although squares and circles produced similar results, the circular configuration allows the grains to freely slide before rigidly locking like the square and triangular setups.

Lastly, the grain size distribution was varied in these experiments by 10 microns in each direction of a set grain size for the tungsten carbide. Although the more important factor is ensuring that the density of the bulk material and therefore the volume fraction is correct when building the geometries, the parametric study did find that there is a slight decrease in the stiffness of the Hugoniot with a higher range of grain size distributions. However, an average grain size was used for simplifying the building of the mono-dispersed particle geometry to accurately portray the dynamic bulk response.

Table 3.3 Results from Parametric Studies from Borg and Vogler's Aspect of Simulating the Dynamic Compaction of a Granular Ceramic

Study	Factor	Affect and Implications
Baseline Response	**Boundary Conditions**	Lateral direction – Periodic or Rigid Wall produces the most accurate results Shock direction – Outflow, since it allows mass to flow in and out of the domain
	Domain Size	The change in the lateral direction by 2 -5 mm did not change the response. Dimensions for the shock direction must be the same as experimental setup
	Mesh Convergence	10 -12 computational cells across the sand grain
Microscale Variations	Hugoniot slope and zero stress sound speed	Variation by 10 percent did not change the bulk response
	Fracture Strength	Variation by 10 percent did not change the dynamic bulk response
	Dynamic Yield Strength and Poisson's Ratio	Increase in yield strength causes a stiffer response. Increase in Poisson's ratio increases HEL
Macroscale Variations	**Initial Volume Fraction**	Increase in volume fraction yields in a stiffer dynamic response.
	Grain Morphology and Grain Size Distribution	Mono-dispersed spheres allows for most accurate dynamic response in comparison to experiments

The summary in table 3.3 shows that the factors in bold is the factors that are important in accurately and reliably simulating the dynamic bulk response of granular heterogeneous materials. Again, these results are for a two-dimensional setup, however these results were followed for three dimensions and provided experimental validation for all of the experiments, as present in *Chapter 5 Results and Discussion*.

IV. FLYER PLATE CASE STUDIES

Three case studies are presented in the following section to validate the use of mesoscale simulations for planar shock or transmitted wave responses. These are listed in order of experimental completion, with the first being the Marquette Brake Pad Shock compaction since it is the oldest of the experiments listed.

The Marquette brake pad experiment helped to develop a simulation method for extracting specific data about individual particles that cannot currently be accomplished from experimental data acquisition. These simulated mesoscale results present distributions of stress and temperature for individual particles. These mesoscale simulations were also the most computationally intensive of the three case studies, providing additional insight into how to resolve grains on the mesoscale.

The Georgia Tech dry sand experiments helped to establish an understanding of what equation of state and strength models to utilize in simulations to represent brittle solid granular materials. Additionally, an example of the difference between stiction and sliding of particles is presented and discussed to help further set a foundation for future mesoscale simulations. These experiments were also compared to other dry sand data to give perspective in the variation of results, even when the densities were similar.

Lastly, the Cambridge dry sand release experiments helped to develop a method for calculating an isentropic release path from planar shock experiments for dry sand by utilizing a combination of theoretical isentropic Mie Grüneisen relationships and mesoscale simulations. These simulations also helped to stress the importance of grain

size and how an average size provides a more accurate dynamic bulk response in comparison to a value not corresponding to this average.

4.1 Marquette Experiment, Brake Pad Shock Compaction

Cullen A. Braun and his advisor Dr. John P. Borg at Marquette University undertook the following experiment. These experiments were setup to determine the differences between sintering brake pad powders using a quasi-static loading process and a dynamic shock consolidation process.

Traditional powder metallurgy is a process of combining powdered material constituents, quasi-statically pressing them into a desired shape and then heating the green compact, in a controlled atmosphere over an extended period of time, in order to bond and weld the granular mixture into a consolidated solid [48]. Dynamic compaction differs from this quasi-static process in that the constituents are rapidly compacted at high strain rates ($> 10^5\ s^{-1}$). The rapid loading from the dynamic compactions causes intra-particle-particle friction, localized plastic deformation and heating, which can lead to elevated temperatures necessary for sintering. Since the dynamic response is completed in much less than a millisecond, there is not time for heat to diffuse and uniformly heat the entire grain system; under these circumstances heating can be confined to the grain surfaces. The advantage of dynamic compaction is that the particle morphology and compacted porosity, as well as the final heat treatment of the welded grain network, can be more controlled in comparison to using a traditional static processes.

The powder mixture of interest contains copper, iron, silica, graphite, molybdenum-disulfide and tin (Cu, Fe, SiO_2, C, MoS_2, and Sn). The consolidated system is a viable, asbestos free, brake-pad material for use in the aviation industry, which are currently manufactured utilizing a quasi-static process. These pads are ideal candidates for industrial scale manufacturing processes given their simple geometry: right circular-cylindrical. One major drawback in utilizing shock consolidation processes is that release waves generated after the shock passes and during unloading can combine in a destructive way to spall the sample. Spall is a quick tensile force that occurs in the direction of the shock, whereas release waves are a representation of stress relief in the material perpendicular to the direction of the shock loading. Release waves are generated at the mold interfaces; thus complicated geometries generate more release waves. However, the focus of this work in this document is utilizing CTH simulations to determine the distribution of Hugoniot state variables for each type of particle in the mixture.

Table 4.1 below presents the mixture constituents along with material properties of interest [15, 33, 41, 49].

Table 4.1 Heterogeneous Mixture Constituent Properties

Mixture Constituents	Percent Volume (%)	Theoretical Density (g/cc)	Particle Size Distribution (μ m)	Solid Density (g/cc)	Hugoniot Slope, s	Sound Speed, C_0 (km/s)	Grüneisen Gamma	Dynamic Yield Strength (GPa)	Shear Modulus (GPa)	Specific Heat, C_V (bar-cm^3 /gK)	Melt Temp. (K)
Copper	18.5	1.65	25<x<100	8.924	0.576	3.940	1.99	0.09	25.6	2.57	1356
Iron	8.2	0.64	50<x<150	7.87	1.481	3.574	1.69	0.18	8.18	3.01	1808
Graphite	8.0	0.17	200<x<400	2.16	1.350	3.650	1.95	0.6	2.26	4.74	>3823
Silica	7.6	0.16	300<x<500	2.197	1.695	0.794	0.90	4.5	0.10	5.02	>1938
MoS_2	1.2	0.06	x<100	4.79	3.050	2.220	1.50	0.16	0.30	1.67	1458
Tin	0.3	0.02	x<125	7.31	1.486	2.608	2.11	0.02	0.14	1.51	505
Mixture		2.71		6.24	0.57	0.475	1.58	0.22	5.9	3.9	
Solid Materials											
Aluminum	N/A	N/A	N/A	2.70	1.351	5.3112	2	540	2.6×10^{-3}	9.6	
Mylar	N/A	N/A	N/A	1.39	1.595	2.2227	0	280	1.3×10^{-5}	1.3	

The porosity of the mixture, defined as the theoretical density of the mixture divided by the solid density, $1-\rho_{00}/\rho_0$, was 0.566 or 56.6%. Simple mixture theory assuming spherical morphologies predicts a theoretical *as-poured* powder density of 2.71 g/cc including the initial porosity and a solid density, in the absence of porosity, of 6.24 g/cc. However, the average experimentally measured poured and tapped density was 2.42 g/cc.

Figure 4.1 below presents the MTS quasi-static compactor apparatus to press the brake-pad powder constituents together and the dynamic experimental apparatus on the left and right, respectively. MTS is a corporation that manufactures material testing machines. The dimensions for the dynamic test schematic are located in table 4.2.

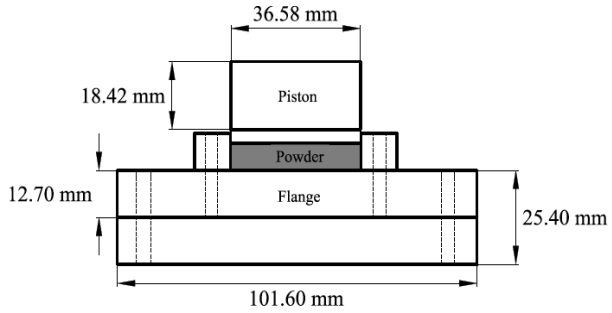

a) Schematic of Quasi-static Test Cell for use with 810 MTS assembly

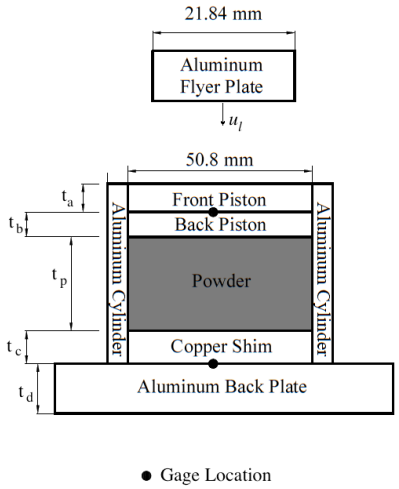

b) Schematic of Dynamic Test Cell. Thickness are listed in table 4.2

Figure 4.1 Experimental Setups

The 9.65 mm thick aluminum flyer plates were polished to a near mirror-finish and launched in a nylon sabot up to velocities of 275 m/s. The projectile velocity was measured using a series of four graphite break-pins. The gun barrel and target chambers were evacuated to pressures below 0.1 torr. The reasoning for the vacuum was to minimize elastic pre-load due to build up of air in the barrel between the flyer and the target [50-52].

Table 4.2 Experimental Flyer Results

Test shot	Initial Density ϱ00 (g/cc)	Launch Velocity *ul* (m/s)	Particle Velocity *up* (m/s)	Shock Velocity *Us* (m/s)	Hugoniot Density ϱ0 (g/cc)	Hugoniot Pressure (GPa)	Front Plate ta (mm)	Back Piston tb (mm)	Powder Thickness tp (mm)	Copper Shim ts (mm)	Back Plate td (mm)
1	2.886 ± 0.055	198 ± 1.96	186 ± 25.0	522 ± 16.0	4.48± 0.085	0.280 ± 0.005	0.8	0.8	1.709 ± 0.055	0.1	25
2	2.712 ± 0.069	241 ± 2.90	208 ± 22.0	641 ± 18.0	4.01± 0.102	0.362 ± 0.009	0.8	0.8	1.820 ± 0.065	0.1	25
3	2.713 ± 0.071	256 ± 3.28	226 ± 23.0	738 ± 21.0	3.91± 0.102	0.452 ± 0.012	0.8	0.8	1.818 ± 0.077	0.1	25
4	2.747 ± 0.077	271 ± 3.68	237 ± 22.0	561 ± 16.0	4.76± 0.133	0.365 ± 0.010	0.8	0.8	1.797 ± 0.078	0.1	25
5	2.724 ± 0.050	263 ± 3.46	239 ± 23.0	537 ± 15.0	4.91± 0.090	0.350 ± 0.006	0.8	0.8	1.812 ± 0.055	0.1	25

Each apparatus consisted of two Manganin strain gages that were encapsulated in Mylar and coated with epoxy. These gages allowed for measurements of transit time and stress levels [50-52], which were then compared to simulations. The locations of the gages are presented in figure 4.1. The back gage was isolated away from the powder with a 0.1 mm copper shim to prevent the powder from destroying the gage at initial impact; this allowed for a longer measurement time.

Each of the powder targets were prepared by pouring a pre-determined mass of the mixture into an aluminum target cylinder while tapping the side of the targets. The front piston is then press fit with the same MTS machine utilized in the static experiments until an initial bulk mixture density of 2.75 g/cc was achieved; the density was determined by the piston displacement. Upon removal from the MTS, the mixture could elastically rebound and displace the piston, explaining the variations in powder densities. The average powder thickness was 1.79 mm.

The computational domain shown in figure 4.2 below, which replicates the experimental setup, presents two lateral dimensions of 4 mm x 4 mm and the longitudinal depth is 5 mm. The domain consisted of approximately 50,000 grains of the constituent powder, which all were assumed to be spherical. The dimensions of the grains were consistent with the average grain diameters from the distributions given in table 4.1.

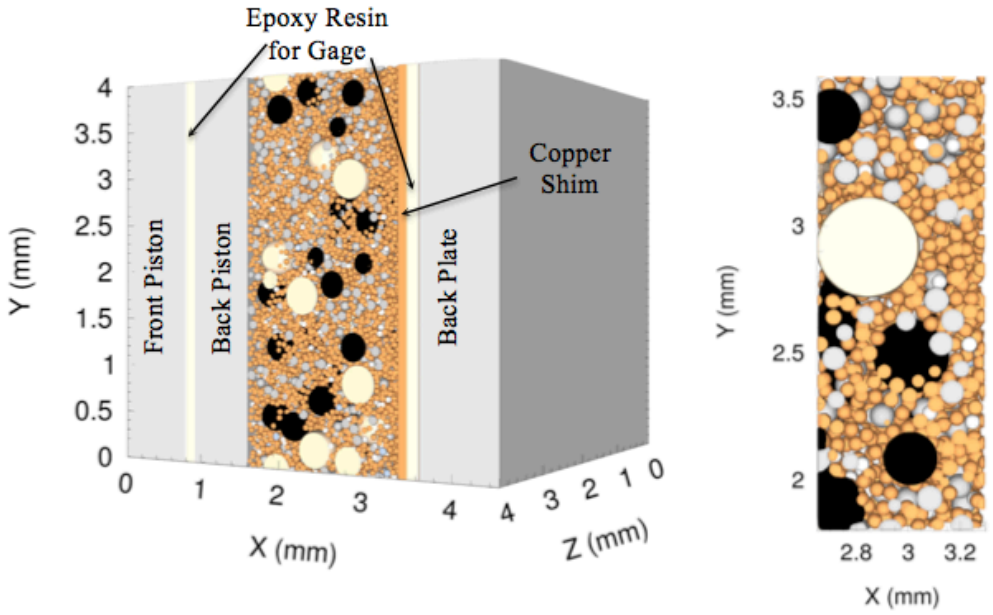

Figure 4.2 Computational Domain for Brake Pad

The particles have been colored by material type: Copper (gold), graphite (black), silica (beige), iron (gray) and the aluminum front and back plate (light gray). Molybdenum disulfide and tin grains are too small to see in the domain.

The domain also consisted of approximately 105 million cells, making these simulations considerably large; to ensure 50,000 cell processes per processor, 67 nodes are needed, as there are 32 processors per node. Like was mentioned in *Section 3.2 Mesoscale Simplification Setup,* the individual material grains were inserted into the computational domain by randomly seeding the domain and growing grains to the experimental volume fraction and average diameter. Additionally, the constituents were modeled with a Mie-Grüneisen equation of state and a Von-Mises yield strength criterion specific to each material constituent. These properties are listed in table 4.1.

The results for these simulations are discussed in *Chapter 5 Results and Discussion* as the methodology for producing these grain on grain interaction results will

be used to help determine the state variables at the Hugoniot state, such as temperature and pressure, of sand and water particles.

4.2 Georgia Tech Experiments, Dry Sand

The Georgia Tech experiments were conducted utilizing a single stage gas gun and a sample apparatus consisting of a copper flyer, a US Oklahoma sand sample encased in a copper cylinder followed by a PMMA backer, which is described in figure 4.2a. The dimensions consisted of a 9.4 mm copper flyer for the lower velocity experiments, 413 m/s and 618 m/s, a 6.25 mm copper flyer for high velocity experiments, 754 m/s and 998 m/s, a 6.25 mm copper driver, a 5 mm US Silica Oklahoma Sand sample, and a 17.6 mm PMMA backer. The US Silica Oklahoma sand for each of the four experiments had an average bulk density of 1.70 g/cc with 35% porosity and being 65% dense. The diameter of the Oklahoma Sand grains varied from 425 to 500 microns, as shown in figure 4.2b, had less than 0.5% moisture content and the grain density was approximately 2.65 g/cc.

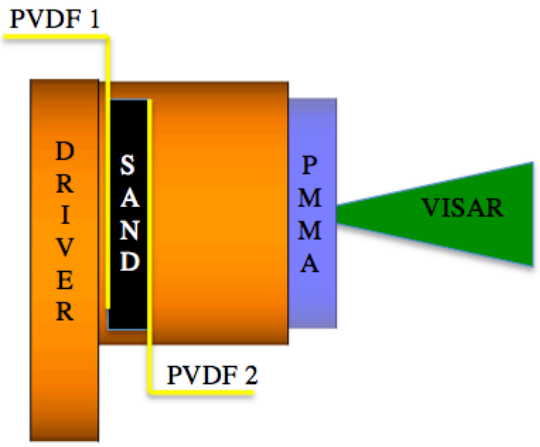

a) Experimental setup apparatus.

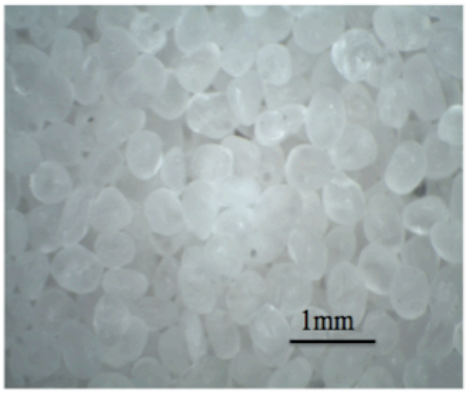

b) Macroscopic photo of the US Silica Oklahoma sand.

Figure 4.3 Experimental Setup and Macroscopic Photo of US Oklahoma Sand

Also, as can be seen in figure 4.3, PVDF gages were placed between the flyer and the sand to measure pressure and calculate shock velocity. A VISAR reading was also taken at the end of the sand sample and the start of the PMMA face to calculate shock velocity with impedance matching. In order for the VISAR to take a reading, the PMMA was sputter coated with a metal microfilm.

Two hydrocodes were utilized in developing the mesoscale models. Both hydrocodes used exactly the same material equations of state and mechanical properties, which are detailed in table 4.3 and table 4.4.

Table 4.3 Mie-Grüneisen Parameters

Mie-Grüneisen Parameter	Quartz	Copper	PMMA
Density, ϱ [g/cm^3]	2.650	8.930	1.186
Zero Stress Sound Speed, C_o [km/s]	3.778	3.940	2.598
Hugoniot Slope, s	2.120	1.489	1.516
Grüneisen Coefficient γ_o	0.9	1.99	0.97

Table 4.4 Mechanical Properties

Mechanical Properties	Quartz	Copper	PMMA
Bulk Dynamic Yield Strength, Y [GPa]	4.1	2.17	0.55
Poisson's Ratio	0.15	0.335	0.35
Fracture Strength, σ_s [GPa] *	5.0	3.38	0.85
Specific Heat, C_v [J/g-K]	0.85	0.393	3.017
Thermal Expansion, α (10^{-6} K^{-1})	8.10	16.4	70.3

*Fracture Strengths were only modeled by CTH, since iSALE does not currently utilize any fracture mechanisms.

It is important to understand that although fracture strengths are included with CTH, this is not the actual fracture but rather is known as spall strength; spall strength is the calculated minimum strength along the hydrostat in the tension direction. Mie-Grüneisen equations of state and simple strength models were used due to proven research that quartz remains elastic in the stress regimes in this study [13, 18].

As with other similar mesoscale simulations, the yielding of the quartz is represented by a von Mises yield strength model [33]. The simulations were carried out with 11 computational cells across each sand grain and each particle was Alpha-Quartz. The Mie-Grüneisen equation of state parameters found from Los Alamos Scientific Laboratory Shock Hugoniot Data (LASL SHD) [41] to obtain bulk sound speed, C_o, and

slope of the Hugoniot, *s*. The Grüneisen Parameter, γ_o , was not included in this this reference; however, by utilizing the following equations and method, the parameter could be calculated as [37]:

$$\gamma_o = \frac{\alpha K_t V_o}{C_v} \quad \text{and} \quad K_t = \rho_o C_o^2 \tag{4.1}$$

where α is the thermal expansion coefficient, K_t is the isothermal bulk modulus, V_o is the initial volume, ρ_o is the initial density, and C_v is the specific heat at constant volume.

The Mie- Grüneisen parameters for copper and PMMA, also known as Plexiglass, were given by parameters found in Asay's and Shahinpoor's GMX-6 Hugoniot Data table [37]. Since fused quartz was the only type of quartz listed in this reference table, other sources were used to determine the parameters for alpha quartz, which is the quartz associated with the Oklahoma Sand. CTH lists parameters for quartz that are populated with a range of particle velocities and placed in a SESAME table [53].

Like ANEOS, SESAME tables are equations of state that are analytically consistent with thermodynamics and develop equations of state for different phases of a material at different loading regimes and in different environments. These parameters are understood to be correct since quartz exhibits a zero stress shock speed and Hugoniot slope of 3.778 km/s and 2.12 respectively under a particle velocity of 1 km/s [25]. This is due to a phase transition of alpha quartz into stishovite above an impact velocity of 1km/s [13]. Yield strength, Poisson's ratio, fracture strength, specific heat and the thermal expansion coefficient for Copper and PMMA were found by utilizing an online database

for mechanical properties; quartz's thermal expansion coefficient was also reported from this database [54].

The yield strength for Copper and PMMA were assumed to be the ultimate tensile strength where failure of the material would occur. For the Yield Strength, it is recognized that quartz is dependent on the Hugoniot Elastic Limit (HEL) [55] with fracture strength of quartz being approximated as the highest value listed for an HEL of quartz. The Poisson's ratio for quartz is taken as 0.15 and the specific heat of quartz is reported as 0.85 J/g/K [13].

iSALE was used to produce 2-D simulations; 3-D simulations were not completed in iSALE due to a complication involving tracer readings. The setup of the simulated experiment is shown in figure 4.4 with the flyer impacting from the top of the domain, the sand placed in the middle of the domain, and the PMMA window fixed to the bottom of the domain. Figure 4.4 is split into two parts to show different materials on the right side with different shading, and a pressure plot on the left side.

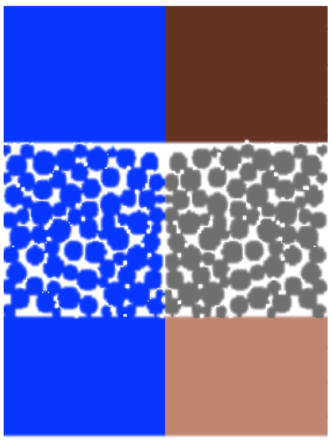

Figure 4.4 iSALE Simulation Setup

The boundary conditions utilized in the experiment treated the sides as a rigid sliding boundary in the longitudinal direction, and a no slip, free surface boundary at the bottom and top of the domain in the latitudinal direction. The sand was allowed to slide in contact with other grains and for mixed boundaries of the sand, the yield strength was set to a constant value of 4.1 GPa, as is listed table 4.4. Only 10 tracers total were placed: 5 equally spaced tracers at the copper driver, sand interface and 5 equally spaced tracers at the PMMA, sand interface.

Fracture strength was not included in this analysis, as the mechanism was not offered in iSALE. Although there are limitations in the iSALE code, the results readily replicated experimental observations. The experiment was scaled down in the latitudinal direction from a 44mm diameter to a 5mm diameter to provide shorter computational time. The longitudinal direction was not scaled, and therefore the shockwave traveled the same distance as in the Georgia Tech experiment. For the dry sand experiments, the particles of quartz were inserted into a void space with an average 450 μm diameter and a varying diameter range of ± 25 μm. iSALE's random particle generator could only produce a 61% dense sand compared to the 65% dense sand in the experiment, which provided a softer response compared to the experiments as will be mentioned later.

For three-dimensional results, CTH was utilized to allow for two different setups. The two setups specified no stiction of the mono-dispersed particles. With stiction, each individual particle welds together during the simulated shock event. With a model including no stiction, this allowed the particles to slide against one another during dynamic loading. The setup can be seen in figure 4.5, where the multicolored grains needed to be specified as different materials for the slide model to be applied in CTH.

The copper driver and flyer are not included in the picture; only the particles representing the sand grains and the PMMA window are included in figure 4.5.

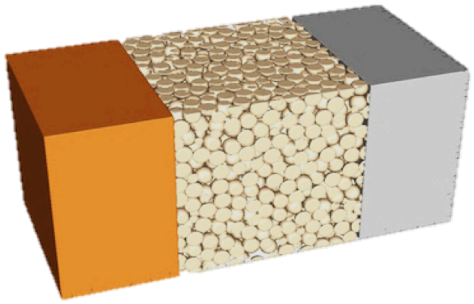

Figure 4.5 CTH Computational Domain

In figure 4.5, the orange-brown block represents the copper flyer, the gray block represents the PMMA window, and the spheres sandwiched between the two blocks represent the Oklahoma sand. The mono-dispersed spheres were created from growing each individual sphere in diameter in a defined volume until it reached the specified volume fraction for each specified density of each shot. Mechanical properties did not vary in the experiments and the densities for each shot were matched with the experimental setups, which are listed in table 4.4 under the results section. Like the iSALE simulations, the 44mm diameter was scaled down to 5mm for shorter computational time.

The boundary conditions consisted of periodic boundary conditions in the axial direction, allowing materials to flow in one side of the sand sample and into the other side of the sand to simulate a semi-infinite medium, a sound speed based absorbing

boundary condition at the interface of the flyer to simulate an infinite medium allowing mass to flow in and out of the system, and lastly an outflow extrapolated pressure condition was applied to the PMMA free surface to allow for material to flow out of the mesh while maintaining a pressure. Ten by ten tracers were evenly distributed at the front center interface of the copper driver and sand; ten tracers in the latitudinal direction and ten tracers in the axial direction were spaced equally apart. For further clarification, this means that a tracer was placed every 0.5 mm to evenly cover the 5 mm by 5mm computational domain. Ten by ten tracers were also placed in a manner similar to the copper driver / sand interface at the PMMA / sand interface.

These results not only showed the differences between two-dimensional and three-dimensional setups, but it also related the importance of utilizing the slide option, which provides more accurate results in comparison to experimental planar shock experiments. Additionally these results tested the Mie Grüneisen equation of state for use with the quartz sand particles as well as test the Von-Mises elastic, perfectly plastic strength model (EPPVM), with the following properties of quartz listed in Table 4.3 and 4.4.

4.3 Cambridge Experiments, Shock Release of Dry Sand

The following experimental setup was developed by the Cavendish Laboratory shock physics team at Cambridge University in the UK [9]. These experiments were setup to understand the complicated non-linear release of sand immediately after the initial shock event. The impact speeds consisted of 800 mps (PMMA flyer), 698, 805,

and 895 mps (Copper Flyer). A PMMA flyer traveling at 800 mps gives a Hugoniot stress and density for the material of interest at a lower regime. This is to allow for a planar shock wave to still occur without edge affects.

Figure 4.6 presents the experimental setup, showing the composition of the flyer, the encasement of the sand, and the location and methods used for data acquisition. The PMMA window in this particular setup shows a cavity, as this type of setup allowed the copper shim to release to a free surface, and therefore obtain a characteristic release of the dry sand. There were other experimental setups involving a solid PMMA window, without a cavity; however, since the purpose of this case study was to emphasize the release of dry sand, these experiments are not discussed or included.

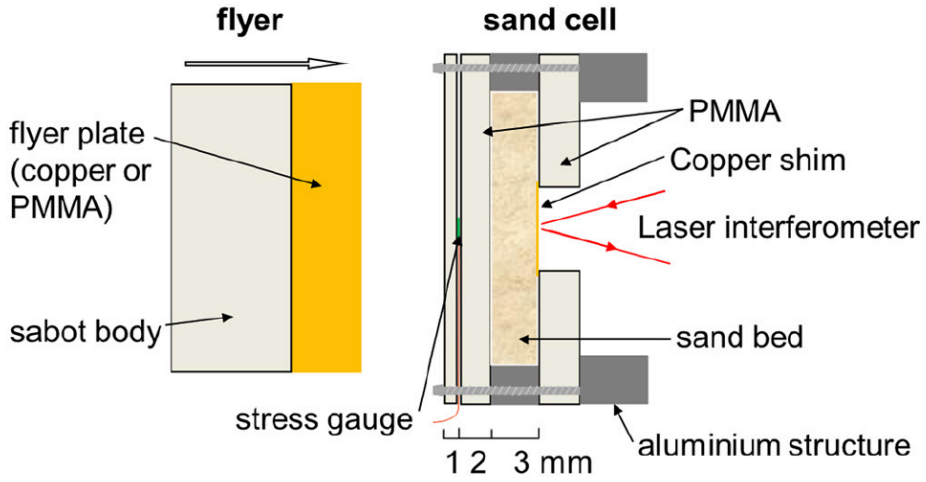

Figure 4.6 Cambridge Experimental Setup [9]

Figure 4.7 shows the setup of the computational domain for the Cambridge release experiments. The difference between the computational domain and the

experiment is that the PMMA window at the back of the copper shim was not included, since there was a hole 3 mm in diameter cut out of it to allow for the copper shim to release. This saved computational space, since using a type 4, outflow pressure extrapolated boundary condition keeps the copper shim at a constant pressure while allowing mass to flow in and out of the domain. Since the computational domain in the latitudinal direction was smaller than this hole, the PMMA was excluded.

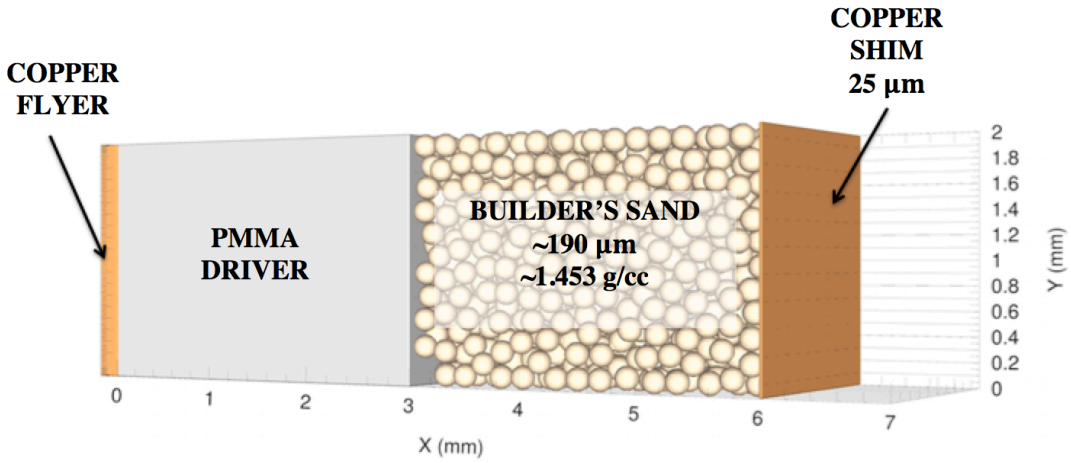

Figure 4.7 Cambridge Sand Release Simulation Setup

In figure 4.7, the domain is 6 mm in the direction of shock (longitudinal direction), with latitudinal dimensions of 2 x 2 mm. In this particular experiment, the material of interest is known as builder's sand, which consists of grains approximately 190 microns in diameter and possessed a packing density of 1.45 g/cc, which is equivalent to a volume fraction of 53 percent. Additionally, as mentioned above, a Mie-Grüneisen equation of state and Von-Misses strength model were applied to the simulation. The yield strength was varied from 4.1 GPa to 4.7 GPa to better match the

experimental results, as in reality Builder's sand is not pure quartz. This change in yield strength is not an accurate measure of the builder's sands properties, but it is one easy method in helping to match experimental results. All the other parameters, such as the slope of the Hugoniot and the sound speed matched the data located in table 4.3 and 4.4.

The PMMA driver was used to help ensure that a planar shock wave developed after the impact of the copper flyer. Additionally, halfway in the PMMA driver was sandwiched a manganin gage encapsulated in epoxy. A 25 micrometer copper shim was included to mimic the experiment, where the reflective surface was utilized to obtain PDV measurements.

CTH tracers were included in the domain to simulate the manganin stress gage, the PDV, as well as to directly determine the particle velocity in the sand. A hundred tracers were evenly distributed and placed at each of these locations, respectively: 1. Halfway into the PMMA driver, 2. Halfway into the sand, and 3. At the back of the copper shim. From these tracers, the data was then compared to experimental data and discussed, which is in *Chapter 5, Section 5.1*. Furthermore, these results allowed for the calculation of the release of the sand from the Hugoniot state utilizing a second law equation which will be discussed in *Chapter 5, Section 5.2*.

V. RESULTS AND DISCUSSION

5.1 Time Traces and Hugoniot Information

This section shows various results for each of the three experiments in this document, as well as results for future possible future experimental setups. The results are specifically related to time traces and Hugoniot relationships from experiments in comparison to simulations. The results will be discussed and compared, as well as a discussion of what possible improvements should be made in order to more accurately depict the dynamic bulk response of the heterogeneous materials.

5.1.1 Marquette Case Study

Manganin strain gage data is presented in figure 5.1, along with both one and three-dimensional simulations. There are two plots, with the one on the left and the right representing the gage near the flyer impact and between the copper shim and the aluminum catcher block, respectively.

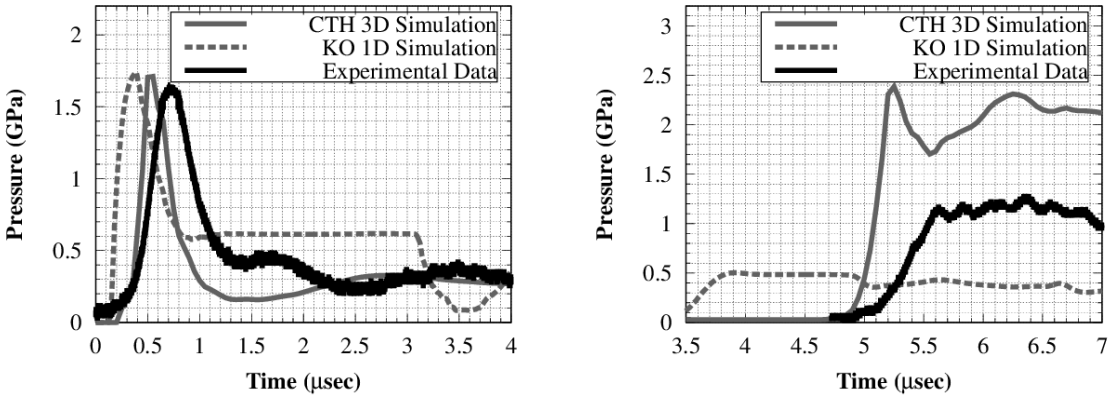

Figure 5.1 Comparison of Incident and Transmitted Gage Data

The results in figure 5.1 are for the shot velocity of 263 m/s and powder density of 2.724 g/cc. There is good agreement between the three-dimensional simulations and the experimental data with regard to the general wave structure and the arrival times. Mr. Braun utilized a one-dimensional hydrocode known as KO to simply model the response in the brake pad to ensure that experimental results were in the correct regime [31]. Unlike mesoscale simulations, KO utilizes a molecular weight based mixture model was used to calculate various bulk properties, known as k_{eff} [38, 56]. The following equations were used to calculate k_{eff}:

$$\frac{k_{eff}}{k_o} = \frac{\sum_{i=0}^{N} \alpha_i \left(\frac{k_i}{k_o}\right) \phi_i}{\sum_{i=0}^{N} \alpha_i \phi_i} \quad \text{where,} \quad \alpha_i = \frac{1}{3} \sum_{i=0}^{N} \left[1 + \left(\frac{k_i}{k_o} - 1\right) g_j\right]^{-1}, \tag{5.1}$$

g_j is a shape factor, which is assumed to be one-third for spherical particles, and ϕ_i is the volume fraction of the constituent. The variable k_o is associated with the greatest volume

fraction of material in the mixture and k_i is the variable associated with the other materials in the mixture. For the brake pad powder, copper was the dominant material by volume fraction and therefore the properties were normalized to copper's material properties. The individual constituents as well as the resulting bulk mixture properties are listed in table 4.1.

Differences in the transmitted gage data in figure 51 are believed to result from local variations in the packing arrangement and morphology of the powder. Although the bulk density of the experiment and simulations match the local density, the density near the gage can vary. The one-dimensional KO simulations underestimate the arrival time and amplitude of the transmitted wave, which is typical of one-dimensional simulations of this type, due to not fully modeling the irreversible processes that are inherently apart of heterogeneous granular materials.

Figure 5.2 presents the static and dynamic experimental results, as well as the three-dimensional CTH simulated results. The results for the static compaction were calculated from the known force given by the MTS and then calculated to a stress since the area of the specimen is known.

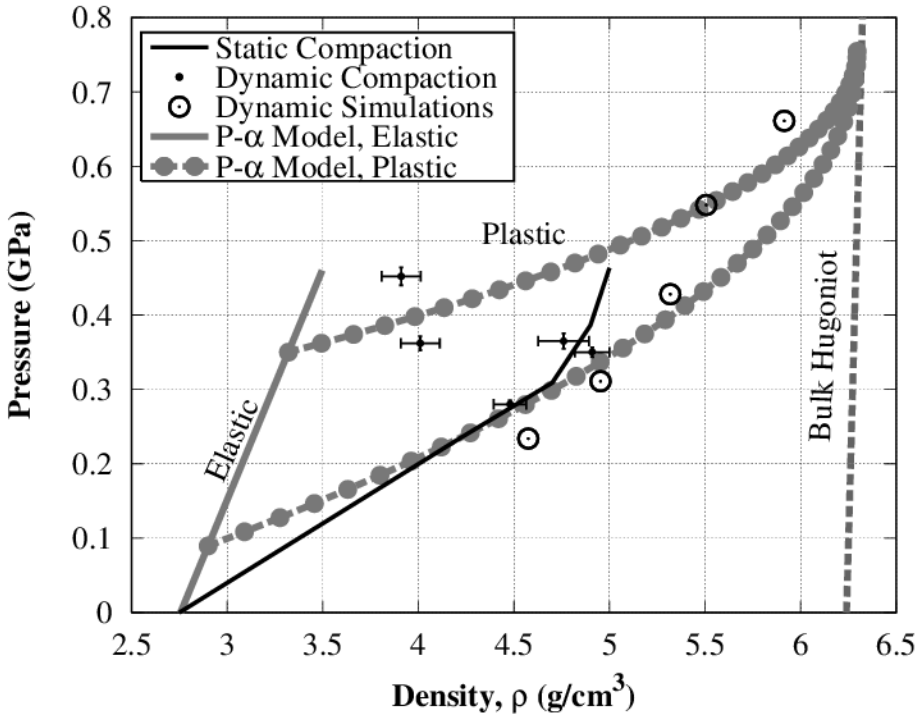

Figure 5.2 Comparison of States Achieved from the Static and Dynamic Tests as well as Three-Dimensional Simulated Results

The dynamic results are different than the quasi-static results in that the compaction follows a linear thermodynamic path, also known as the Rayleigh line. Additionally, it is hard to accurately calculate the density at higher static compaction results due to gases trapped in between grains after pore collapse. From the times series data presented in figure 5.1, a pressure and density state were inferred by utilizing impedance matching. The compaction wave speed, U_S, was determined from the difference in arrival times from the front and back pressure gages. Using equation 2.5, a linear line fit to the experimental data can be given to give a Hugoniot slope of 0.569 and a zero stress sound speed of 475 m/s.

The p-alpha model was included in figure 5.2 to show a range of compaction values. Both the computational and experimental data fall in the general range of the p-alpha model. However, there is a discrepancy between the computational and experimental data. It is assumed that the experimental data was not accurate in that the material compaction could be different, hence the reasoning behind including the p-alpha curve. Computational data shows a Hugoniot that is comparable to other heterogeneous dynamic bulk responses. The difference in the results does not detract from the results obtained in *Section 5.3 Histogram Analysis*, which delves into the interaction of particles at the surface of grains.

The particular Hugoniot results associated with this case study highlights the differences between the p-alpha model and mesoscale simulations. Although the p-alpha model presents a range of values that the experiment could possibly fall under by giving a minimum and maximum fitting parameter values, mesoscale simulations look at each material particle and determine how individual impedance mismatches affects the overall dynamic response. This becomes important when analyzing the temperatures and stresses of the individual particles, as will be done in *Section 5.3, Histogram Analysis*.

5.1.2 Georgia Tech Case Study

The Georgia Tech case study provided an overall setup process for planar shock wave experiments, in that these studies provided the foundation for understanding how Hugoniot information can be obtained in an experiment. These results also tested iSALE in comparison to CTH and helped to create an understanding of the difference in having

CTH's slide command off or on during a shock event. These results helped then to verify the finding of the interactive behavior between particles for further helping to validate mesoscale simulations in comparison to experiments.

As mentioned before, iSALE is an open source hydrocode that was used in order to compare its capabilities to the capabilities of CTH. Figure 5.3 presents a comparison of iSALE 2-D simulated results versus Georgia Tech experimental VISAR results. As expected for a smaller density than the experiment's density, the arrival time of the shockwaves for each simulation compared to the experimental results is greater and also manifests a softer response. While the experiment's densities were on average of 1.70 g/cc (65% dense), iSALE's density was 1.63 g/cc (61% dense). Unlike CTH where the geometry is created from the program "Mesogrow" or LAMMMPS, iSALE utilizes a random particle generator that can only pack to densities of approximately 61 percent, presenting a "softer" Hugoniot response, which is shown in figure 5.5. A newer version of iSALE has made improvements to performing mesoscale simulations. Figure 5.3 below shows that the peak particle velocity values of the iSALE results do not match due to this lower sand density creation.

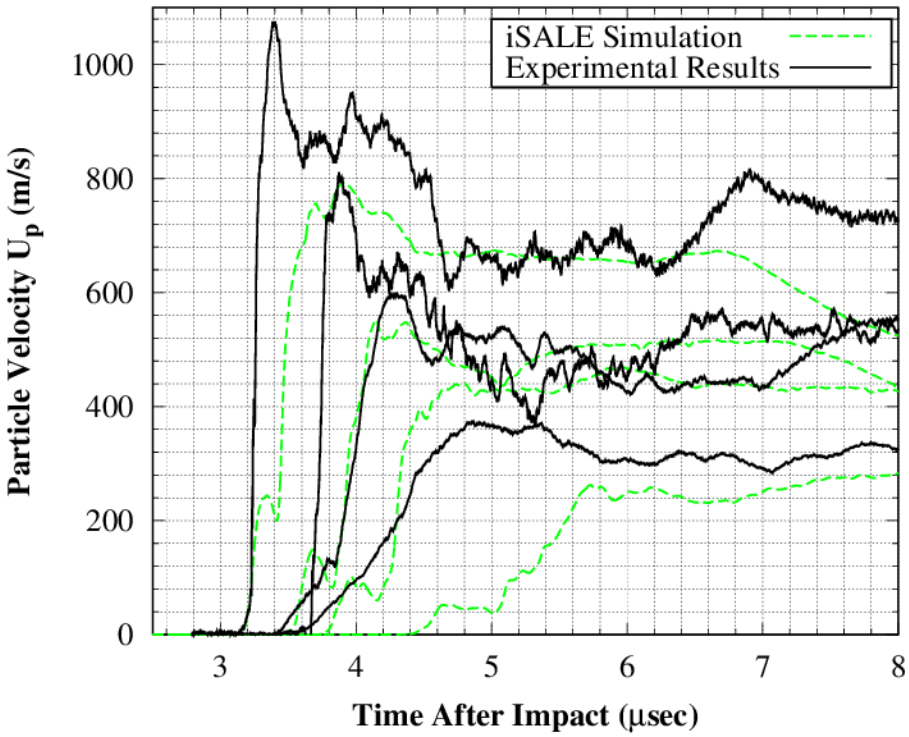

Figure 5.3 iSALE Simulated VISAR vs. Experimental VISAR

The flyer impact speeds in figure 5.3 increase from right to left on the plot and the dotted green lines represents the simulated results. Averages of these iSALE peaks were taken and then by theoretical impedance matching, the resulting particle velocities in table 5.1 were calculated and utilized to create a Hugoniot.

In figure 5.4, there are three comparisons of CTH 3-D simulated VISAR readings. Figure 5.4a and 5.4b show the simulated results versus the experimental results, one without stiction and the other with stiction, respectively. Figure 5c shows the comparison of the simulations with the different particle interactions choices. Figure 5a shows a much softer response than figure 5b, since the particles might move against each other and dissipate energy; this behavior is not usually accounted for in the models that treat dry sand as a homogeneous material. The heterogeneity of the granular material is not

noticed by the fluctuations in figure 5a compared to figure 5b since there are more interactions among the sliding particles compared to the welded particles. There is a wide range of variation in the plateaus of the particle velocities of both types of simulated results (figure 5c), with the simulations with stiction possessing higher particle velocities than the simulations with stiction. As will be seen in figure 5.5 of the Hugoniot results, the simulated results without stiction, or the slide option, obtains a much more accurate result in comparison to the experiments than the over predicted and stiffer response of the stiction or welded model.

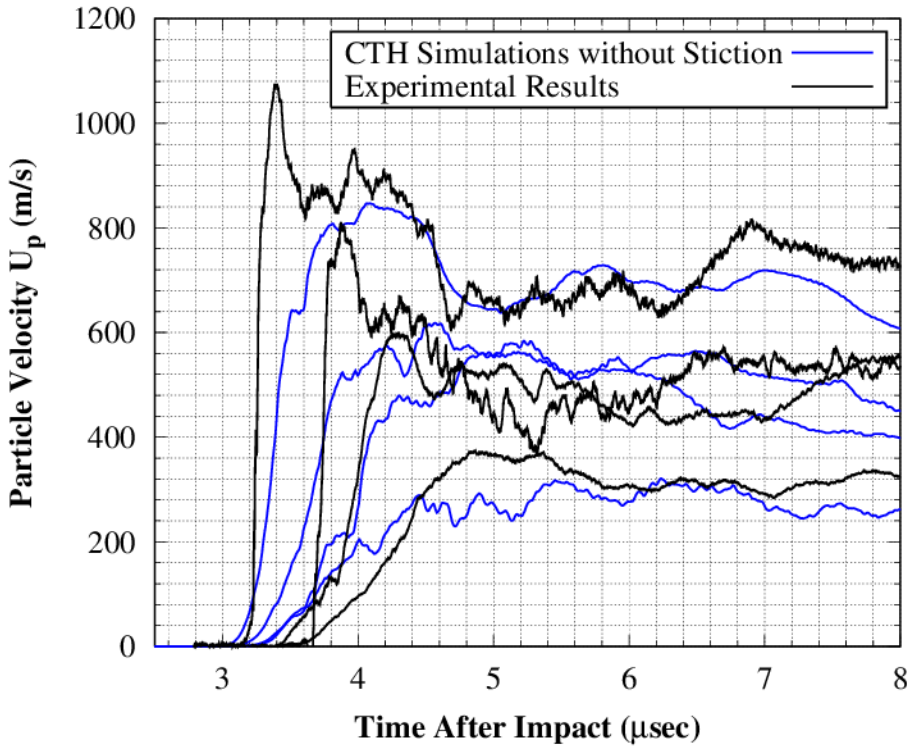

Figure 5.4 a) CTH Simulations Without Stiction VISAR versus Experimental VISAR

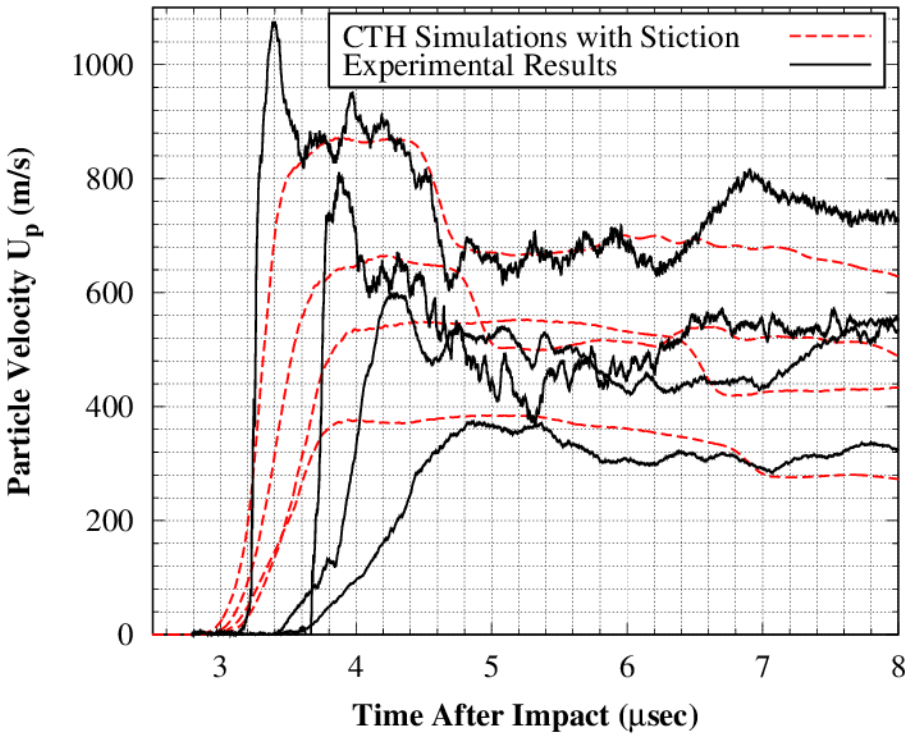

Figure 5.4 b) CTH Simulations With Stiction VISAR versus Experimental VISAR

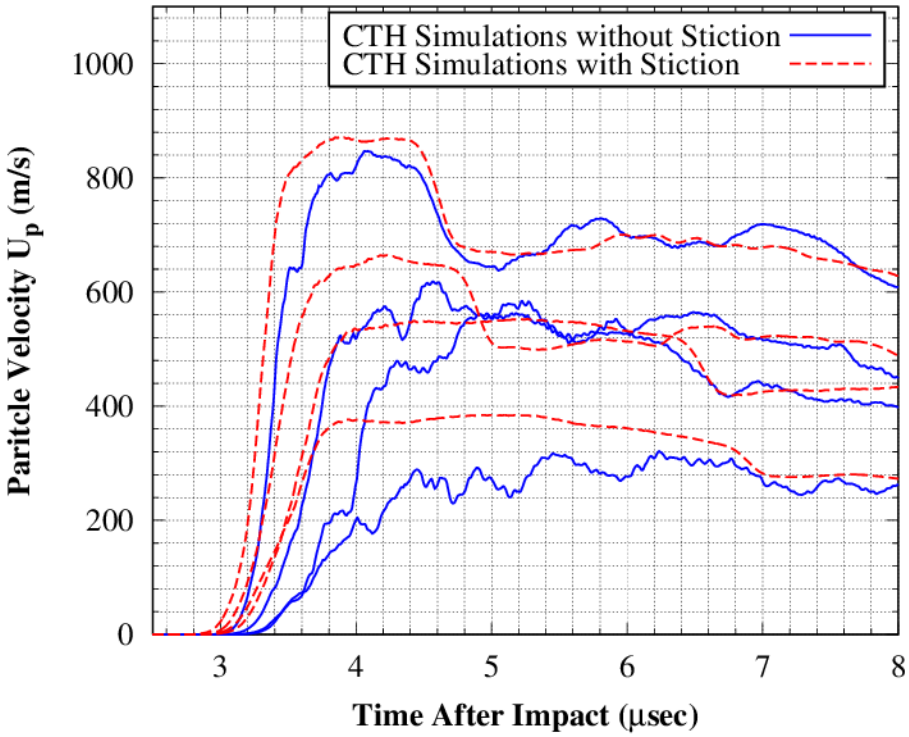

Figure 5.4 c) CTH Simulations Without Stiction versus With Stiction VISAR

Table 5.1 lists all of the results from the experiment as well as the simulations. Particle velocities (Up) were calculated by averaging the plateaus of the VISAR readings in figure 5.3 and figure 5.4a, 5.4b, and 5.4c. Theoretical impedance matching was then utilized to find the particle velocity at the copper driver, sand interface. Shock velocity (U_s) was calculated by using the following equation:

$$U_S = \frac{\Delta x}{(t_{VISAR} - t_{PVDF1})}, \tag{5.2}$$

where the Δx is the thickness of the sand sample, t_{VISAR} is the time of the midpoint of the VISAR's initial shockwave arrival, and t_{PVDF1} is the time at midpoint of the input PVDF gage's shockwave arrival. From the calculations of Us and Up, a Hugoniot slope and bulk sound speed were calculated and given as Hugoniot equations next to each area of interest. The simulated model with stiction has the sharpest and stiffest response with the highest calculated shock speed and iSALE has the softest response with the lowest calculated shock speed.

Table 5.1 Initial Densities and Results

Impact velocities are 413 m/s, 618 m/s, 754 m/s, and 998 m/s			
Experimental Results			
Initial Density, ρ (g/cm^3	Particle Velocity, Up (m/s)	Shock Velocity, Us (m/s)	
1.76	382	1620	Us=1.78Up+924
1.71	570	1939	
1.72	678	2100	
1.73	899	2547	
iSALE 2D			
Initial Density, ρ (g/cm^3)	Particle Velocity, Up (m/s)	Shock Velocity, Us (m/s)	
1.63	398	1267	Us=1.93Up+529
1.63	588	1690	
1.63	701	1923	
1.63	928	2293	
CTH 3D without Stiction			
Initial Density, ρ (g/cm^3)	Particle Velocity, Up (m/s)	Shock Velocity, Us (m/s)	
1.76	397	1817	Us=1.41Up+1201
1.71	583	1948	
1.72	692	2169	
1.73	917	2532	
CTH 3D with Stiction			
Initial Density, ρ (g/cm^3)	Particle Velocity, Up (m/s)	Shock Velocity, Us (m/s)	
1.76	378	2462	Us=0.28Up+2285
1.71	558	2381	
1.72	672	2397	
1.73	888	2598	

After the results were found in table 5.1, Hugoniots were created to interpret the data from the simulations to experimental results. Figure 5.5 shows each of these setups with the individual shots represented by different shape markers. The Hugoniot lines are created over a range of particle and shock velocities with constant sound speeds, Hugoniot slopes, and initial densities from table 5.1, to find Hugoniot stresses and Hugoniot densities. The solid quartz Hugoniot is also on figure 5.5 with an initial density of 2.65 g/cm^3 to present a baseline understanding of a homogenous material

compared to a porous, heterogeneous material. The softest response of the simulations is the 2D iSALE results, not only because of a low-density value of 1.62 g/cm^3, but due to non-existent axial particle contact that are not taken into account with a 2D calculation. A 3D calculation allowed for sliding of the particles during dynamic compaction to produce the most accurate results providing a similar Hugoniot fit to experimental results.

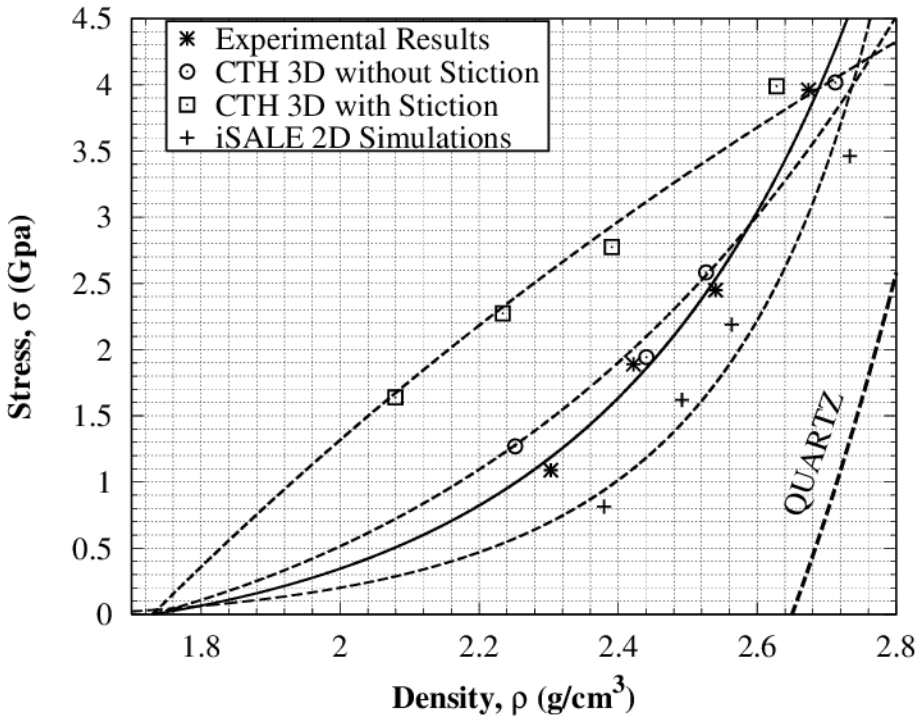

Figure 5.5 Georgia Tech Hugoniot Results

The variation in this experiment is most likely due to selection of mechanical properties and the assumption that the particles are spherical in nature rather than representing a more characteristic sand geometry, such as a rhomboid or ellipsoid. The

selection of the geometries and the mechanical properties make a difference in how accurate and reliable the simulations are for a planar shock impact experiments.

Variation in dynamic bulk response for dry sand is not uncommon as is presented in figure 5.6.

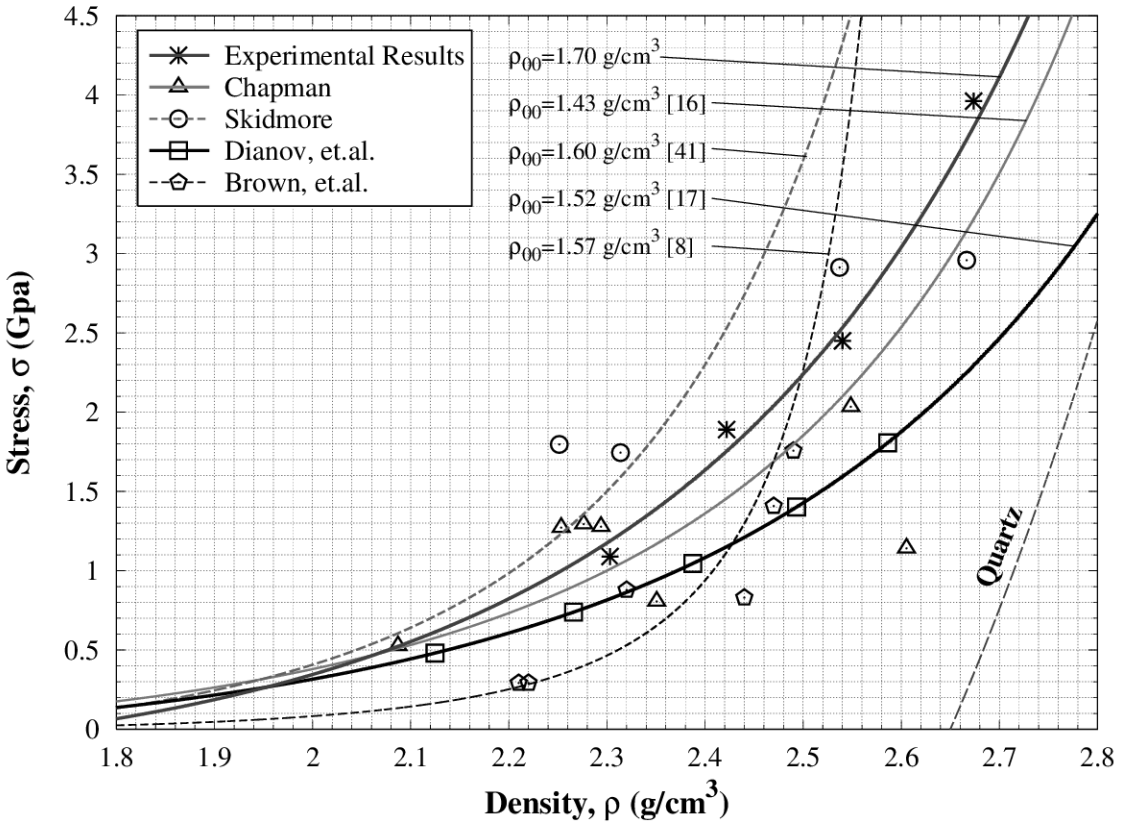

Figure 5.6 Comparison of Dry Sand Hugoniots to the Georgia Tech Case Study

As has been discovered from mesoscale simulations, these variations are most likely occurring due to grain morphology, the variation in volume fraction occupied by the sand particles, and the size of the sand grains. This understanding further stresses the

importance of ensuring if mesoscale simulations are to be validated by experiments, these variables must be correct. Notice that even for similar sand densities, the response is still slightly varied; this can be explained by different methods for calculating the Hugoniot from experiments, as this will causes variations in the linear fit Us-Up data utilize to create Hugoniots in stress, density space.

5.1.3 Cambridge Case Study

The following results from the Cambridge experiment [9] help to validate the simulations done in CTH and present shock release information for dry sand. Although the case study of the Cambridge Experiments focused on release, these results also present information on the comparison of stress and PDV, as well as how the data changes with variation in grain size.

Figure 5.7 shows both three-dimensional CTH simulations and experimental data on one plot. Stress is on the left side and particle velocity is on the right side. The blue line is CTH data taken from tracer data, as mentioned in the experimental setup in section 4.3, Cambridge Shock Release, and the black and red lines are experimental Manganin Gage and PDV data, respectively. The experimental results are for a copper flyer traveling at 895 mps.

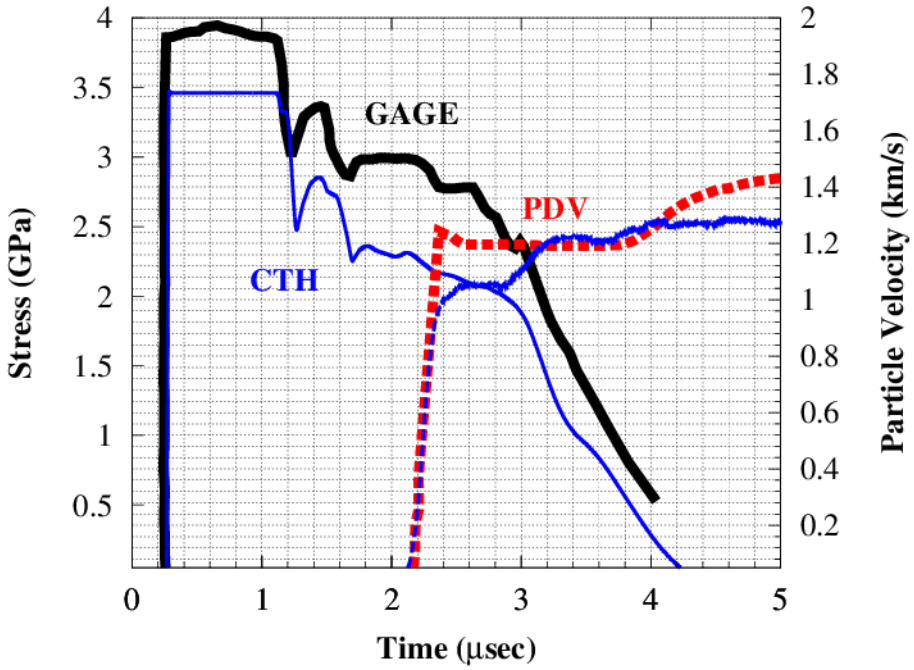

Figure 5.7 Cambridge Experimental Data Versus Simulation

Notice, there is disagreement in figure 5.6 in comparison to the simulated data. The strength model used was Von Mises, and it is hypothesized that the HEL set at 4.7 GPa is too low, as a higher HEL would better match the plateaus for the experimental PDV and GAGE data. This does not mean assumption of assuming the Builder's Sand had pure quartz properties should be relaxed when simulating possible future experiments with Builder's sand, but rather incorporating a higher HEL for more accurate simulations with this assumption. Other factors were included, such as the "SLIDE" option and a fracture strength of 5.1 GPa were set, as these values correspond to the findings of the Borg and Vogler's paper, as described in the *section 3.5 Sensitivity Analysis*.

The Hugoniot stress in figure 5.7 corresponds to the dip that occurs past the first plateau in the gage. By averaging the second plateau, an average bulk Hugoniot response of the sand can be obtained. For the particle velocity that corresponds to the Hugoniot

state, an impedance matching method must be done since the PDV is reflecting off of a 25 micron copper shim. By knowing the thickness and density of the copper shim, and the density of the sand, a particle velocity at the Hugoniot state for the sand can be obtained from the experimental results.

Particle velocity profiles from CTH simulations can be taken directly from tracers placed in the middle of the sand bed, and the corresponding Hugoniot particle velocity is equal to the first plateau as measured by the tracer. In order to obtain a bulk dynamic response of the sand, a hundred tracers were evenly inserted perpendicular to the shot direction across the sand domain and averaged to obtain one overall trace. This trace is a representative average at the Hugoniot state of the dry sand at one instance in time. Spatially there is large variation in particle velocity as a result of grain interfaces and void space. These results from the simulated gage data and the tracer information were then plotted in figure 5.8 against other shot speeds.

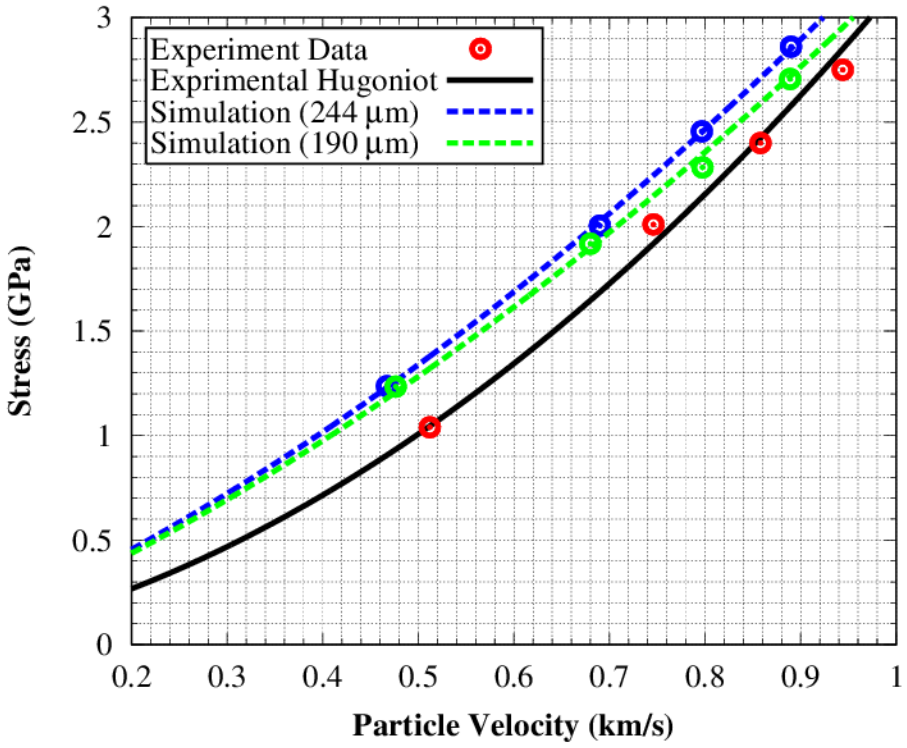

Figure 5.8 Cambridge Hugoniot Results Compared to Simulation

The first shot corresponding to the farthest left red dot in figure 5.8 was accomplished by using a PMMA flyer instead of a copper flyer at 800 mps to allow for a smooth planar shock wave at lower velocities. The last three red data points going from left to right were done with a copper flyer at 594, 805, and 895 mps respectively. The blue and green data points and lines correspond to simulated data and its respective Hugoniot information. As was mentioned in Chapter 3, the grain realization for the 244-micron sand was developed using LAMMMPS and was at the same volume fraction as the 190-micron sand, which used Mesogrow. Although the size of the sand grains for the LAMMMPS did not match the average grain size, it further stresses the importance that

grain size influences the dynamic bulk shock response of the sand at higher flyer velocities.

By keeping the volume fraction constant and decreasing the grain size the Hugoniot particle velocity and stress decreases, but the Hugoniot shock speed increases. This is consistent with studies found by Jeff Lajeunesse's *Simulating the Planar Shock Response of Concrete* [3] where the size of the sand grains in the Concrete matrix changed the dynamic response of the material. The aggregate was held at a constant volume fraction, but by changing the size of the sand grains, the same relationship mentioned above occurred; decreasing the size of the sand grains decreased the overall bulk response of the material. Other research in the area of different grain sizes affecting the dynamic bulk response is currently being done at Georgia Tech, where similar results have been found. Further research in this area will be discussed in *Chapter 6*, *Future Work*.

5.2 Release Information

The following information includes experimental and simulation release comparisons for the Cambridge case study. Although there are other methods for calculating the release of materials from reverse ballistic shots and other setups [3, 15], this is an attempt to discuss release for planar shock experiments. Additionally, this information helps to further characterize the dynamic bulk response of sand as well as setup a discussion for future release of other heterogeneous granular materials, like

water-saturated sand. The release of a material is a measure of the irreversible nature of planar shock experiments of heterogeneous materials.

5.2.1 Cambridge Case Study

For the Cambridge case study, the experimental release was found by understanding that the copper shim in which the PDV was measuring from releases to free space during the shock event. Once the first set of shock waves are released to free space, the second set of shock waves travel from that free space back into the sand bed. Because of this behavior, the free surface velocity points are then reflected about their perspective Hugoniot points to give a theoretical release [9].

As the paper goes on to mention, this information does not give an accurate portrayal of the release path, as it only measures one velocity of the final release to free space. In order to characterize a path of release states leading to the final release state for planar shock experiments, a couple of techniques are needed. Release states are hard to find in planar shock experiments due to the limited thickness of the copper shim. The copper shim has "rung up" so fast that release states are hard to determine. However, if the copper shim is too thick, the PDV does not pick up high resolutions beats and the data does not accurately portray the shock event of the sand.

Nonetheless, the current technique adopted in the Cambridge case study works well in calculating the release path by assuming an isentropic relationship, as will explained later in this section. The experimental release behavior can be observed in

figure 5.9 corresponding to the red lines. The copper flyer traveling at 805 mps was not included in this graph, as to not overlap with the 895 mps shot.

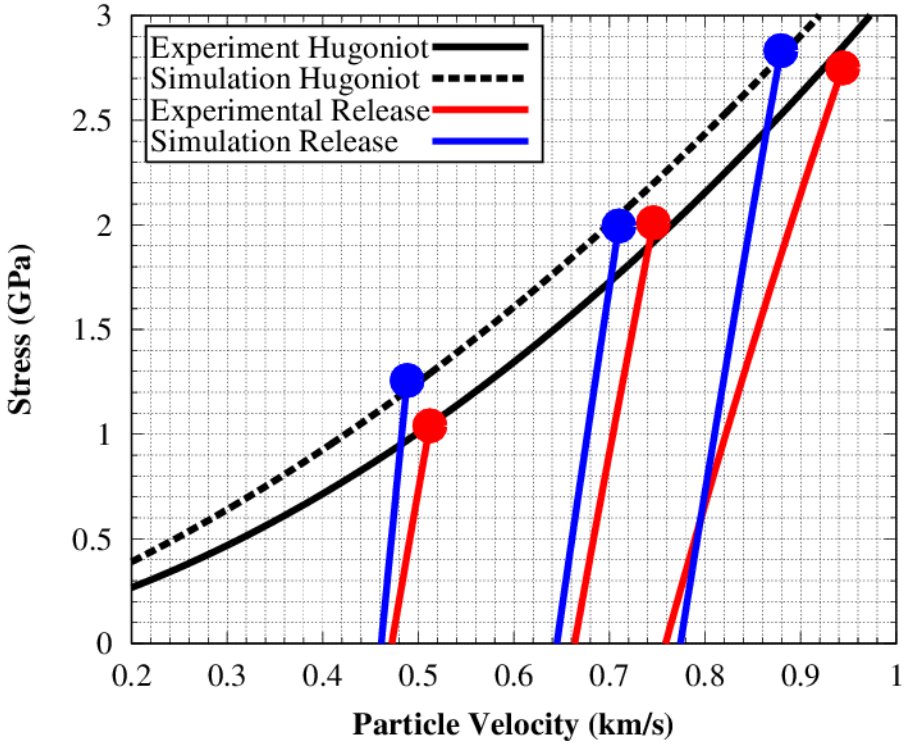

Figure 5.9 Cambridge Release Data Compared to Release from Simulations

For the simulated release paths, a couple of assumptions were made in order to accomplish this calculation. By assuming that the release is isentropic to final release, and a Mie Grüneisen equation of state is used to characterize the sand, the release in Stress-Particle Velocity space can be found by numerically integrating the Riemann integral [57, 58]:

$$U_p - U_{p,H} = \int_{V_H}^{V} \left[-\left(\frac{\partial P}{\partial V}\right)_s \right]^{\frac{1}{2}} dV \tag{5.3}$$

$$\left(\frac{\partial P}{\partial V}\right)_s = \left(\frac{\partial P_H}{\partial V}\right)\left[1 - \frac{1}{2}\gamma_o\left(1 - \frac{V}{V_o}\right)\right] + \frac{\gamma_o}{2V_o}P_H - \frac{\gamma_o}{V_o}P \tag{5.4}$$

Integrating equation 2.4 assuming constant entropy with respect to specific volume derives equation 5.4. The internal energy terms in equation 2.5 are substituted with equation 2.3 in order to be in terms of specific volume to obtain a different version of the Mie Grüneisen equation of state:

$$P = P_H + \frac{\gamma_o}{2V}\left[(P + P_H)(V_o - V)\right] \tag{5.5}$$

It should be noted that subscripts with *H* correspond to the Hugoniot state and *o*, correspond to the initial value before the shock loading occurs. For $\frac{\partial P_H}{\partial V}$, equation 2.8 can be utilized by substituting equation 5.6 for U_p [39]:

$$U_p = \frac{C_o(V_o - V)}{V_o - s(V_o - V)}. \tag{5.6}$$

After substitution, equation 2.8 becomes:

$$P_H = \frac{C_o^2}{V_o}\left[\frac{(V_o - V)}{V_o - s(V_o - V)} + s\left(\frac{(V_o - V)}{V_o - s(V_o - V)}\right)^2\right] \tag{5.7}$$

Now that all of the equations are defined, the Riemann Integral needs to be solved in order to determine release. In order to solve the Riemann Integral, equation 5.3, a 4th order Runge Kutta scheme can be done to calculate a locust of release path points all the way to an ambient pressure, in this case 0 GPa. These theoretical simulation paths for each shot of the Cambridge Case study fall close to the technique utilized by Dr. Braithwaite and his team.

5.3 Histogram Analysis

The following analysis is utilized in looking at interactions between grain surfaces for both the baseline Marquette Brake Pad Shock Compaction. As far is known, these results are only possible with the utilization of mesoscale simulations with hydrocodes, as this observance in particle interaction and distribution of energy would be hard to calculate if the material were treated as a bulk material with fitting parameters, like the p-alpha model. Finite element and peridynamic codes do not use equations of state to give information for state variables (i.e. stress, temperature, density, etc), and therefore cannot determine the rise in temperature of the materials or the contact points that causes

sintering of the grains. The presented analysis is not possible with current experimental techniques, as it provides insight into how grains interact during a shock event. The results are discussed and presented utilizing histogram techniques and visually represented with CTH SpyMaster plots.

5.3.1 Marquette Case Study

Figures 5.10 and 5.11 present two-dimensional sections from the three-dimensional simulations of the longitudinal stress and temperature fields respectively. Each figure shows two different instances in time, where a) is the stress and temperature distribution after the initial shock has passed, also known as the Hugoniot state. The figures on the left, b), illustrates stress and temperature distributions after the re-shock has interacted with the rear surface, which increase both stress and temperature.

Although figure 5.10 presents this process with little to no observable additional deviatoric deformation of individual grains, this is because of the design of the experiment. The experiments are fundamentally one-dimensional, since each subsequent reflected stress wave tends to make the stress field more homogenous as the target "rings" to a final steady state. This is because once the material has yielded, the local stress must be in equilibrium across surface boundaries.

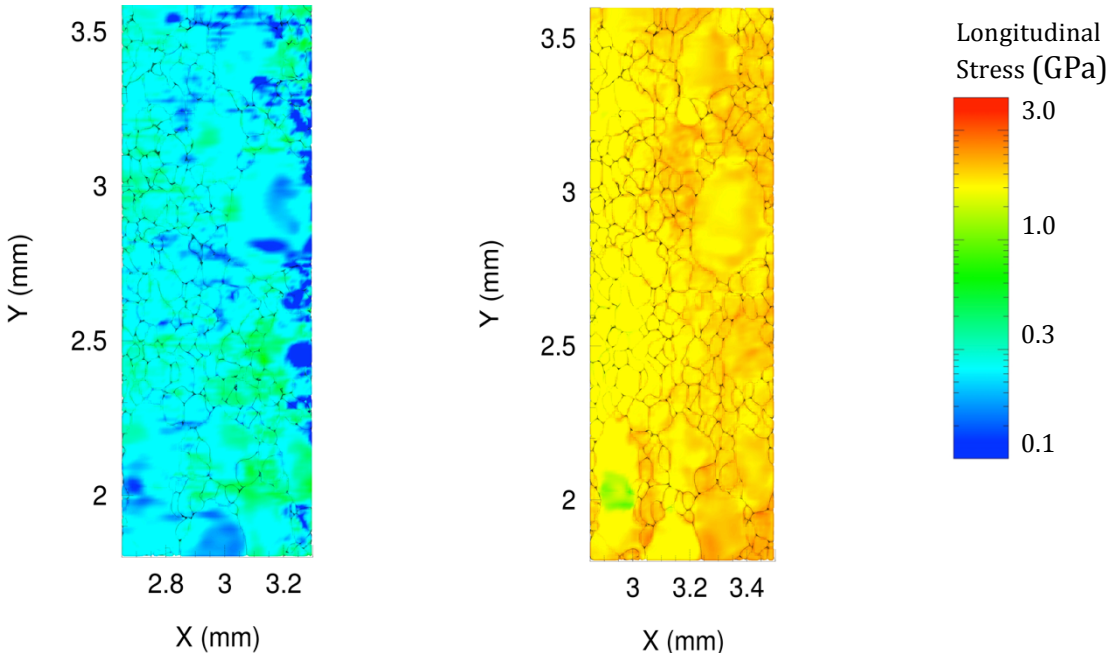

a) Longitudinal stress after initial shock at 4.6 μs.

b) Longitudinal stress after re-shock at 5.6 μs.

Figure 5.10 Two-Dimensional Section of Longitudinal Stress at Two Instances in Time for Impact Velocity of 263 m/s

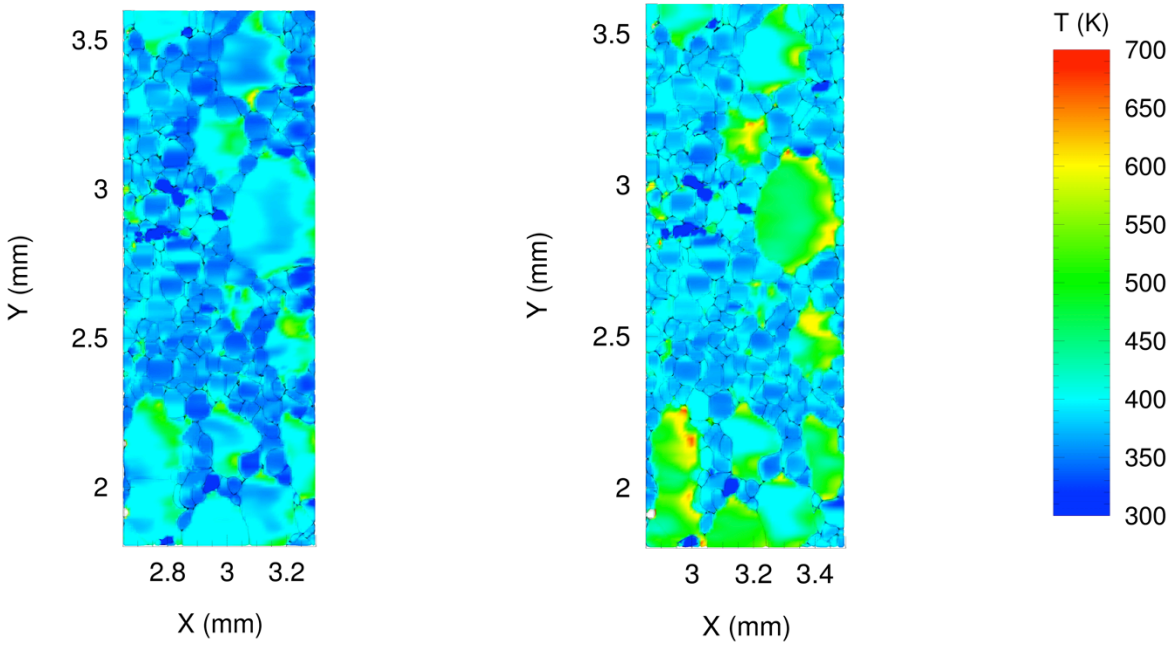

a) Temperature after initial shock at 4.6 μs.

b) Temperature after re-shock at 5.6 μs.

Figure 5.11 Two-Dimensional Section of the Temperature Field at Two Instances in Time for an Impact Velocity of 263 m/s.

For figure 5.11, higher temperatures are concentrated along the contact surfaces of particles where the material impedance mismatch is largest. It is also noticed that temperature variations are highest along contact surfaces where the normal stress and shear deformations maximize local plastic work. In experiments, as the normal and shear stress is increased, irreversible processes increase the local temperature. However, CTH models internal energy and therefore calculates temperature with a simple relationship as follows [39]:

$$E = C_v \Delta T . \tag{5.8}$$

This limitation does not accurately calculate the heat transfer from inter-particle friction as is seen in actual experiments. Nonetheless, the results help to depict the relationships found between grains and suggest further research efforts in this area.

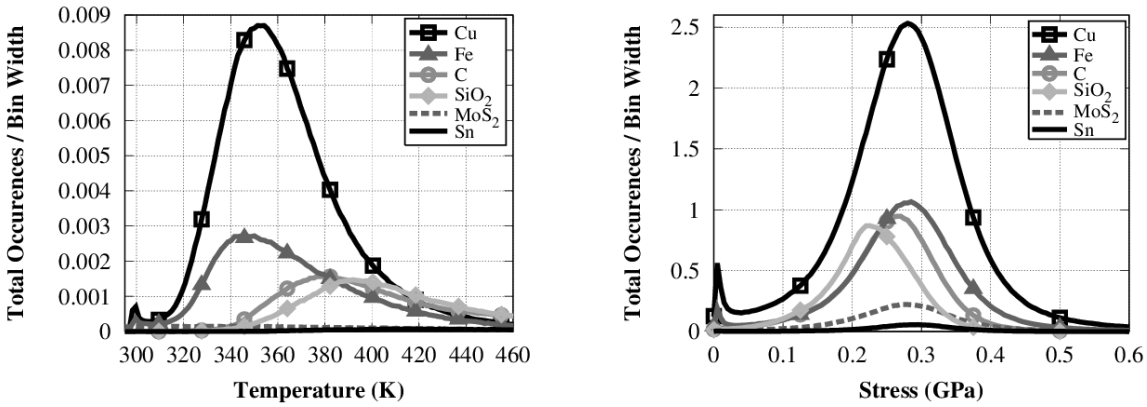

a) Temperature Distribution. b) Stress Distribution.

Figure 5.12 Simulated Temperature and Stress Distributions at 4.6 μs of the Total Powder at the Hugoniot State for an Impact Velocity of 263 m/s

Figure 5.12 above presents both the temperature and stress distributions of each constituent in the powder at the Hugoniot state. Interestingly, stress equilibrium requires the normal stress be constant across a particle interface. As a result, the peak stresses of the individual constituents in figure 5.12 b roughly correspond to the Hugoniot stress presented in figure 5.1. However, there is no similar equilibrium requirement on temperature, thus presenting the peak occurrence of temperature differs slightly for each constituent. This temperature difference is strongly dependent on the equation of state (EOS) selected. The most likely occurrence for copper and iron, which are the greatest constituent volume fractions in the powder mixture, occurs near 350K. This is not close enough to the melt temperatures to effectively sinter this mixture.

It might be possible that from reshock of the material, the temperature can be driven higher, as shown in figure 5.13. It should be noted that the melt temperatures of copper and iron at atmospheric pressure are near 1358K and 1811K respectively.

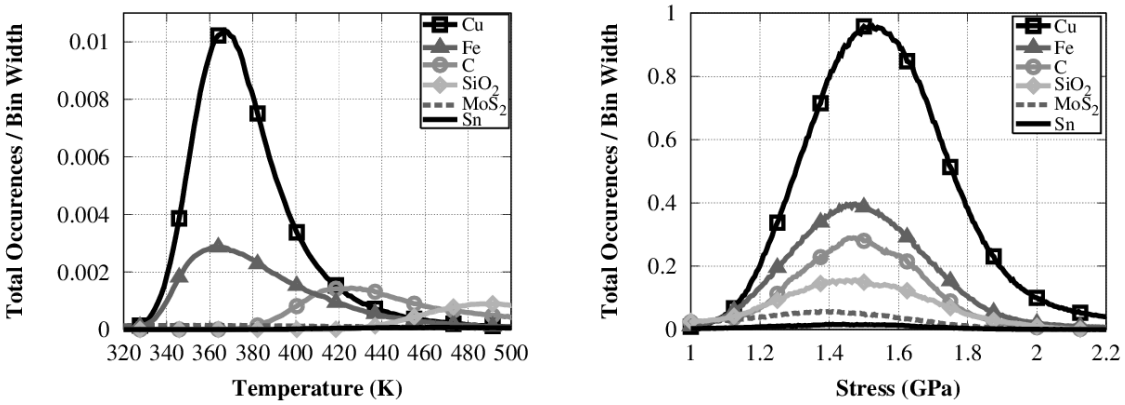

a) Temperature Distribution. b) Stress Distribution.

Figure 5.13 Simulated Temperature and Stress Distributions at 5.6 μs of the total powder immediately after re-shock for an impact velocity of 263 m/s.

In order to determine the flyer velocity needed to achieve higher temperatures in the iron and copper, and subsequently initiate diffusion and welding of these particles, Hugoniot temperature can be calculated utilizing the following equation [39]:

$$C_v \left(\frac{dT}{dV}\right)_H + \frac{\gamma T C_v}{V} = \frac{1}{2}\left(\frac{dP}{dV}\right)_H (V_o - V) + \frac{P}{2} \qquad (5.9)$$

where γ is the Grüneisen parameter of the bulk material, C_V is the specific heat and V is the specific volume. The initial conditions are taken to be the ambient temperature, T_0 being 298 K and the initial specific volume. The particle velocity calculated from equation 5.9 which is necessary for the mixture to achieve at least the melt temperature of copper, 1350 K [52], is 950 m/s. By impedance matching the velocity back to the flyer, the launch velocity of the flyer must be approximately 800 m/s. Achieving these

velocities is beyond the capability of the gun system that was utilized by Mr. Braun; however, it may be simulated.

Figure 5.14 presents the temperature and pressure distributions at Hugoniot state for an impact velocity of 800 m/s. As predicted by equation 5.3, the melting of copper and iron does occur, suggesting that impact velocities above 800 m/s would be sufficient for localized welding and sintering of the material. The highest temperatures, like before, are concentrated at the grain surfaces, and the high impedance mismatch between the quartz and the iron and the copper grains show the greatest temperature increase.

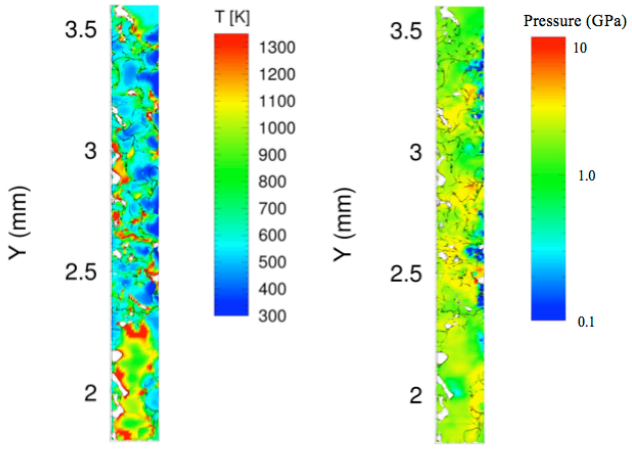

Figure 5.14 Two-Dimensional Section of the Temperature Field of the Material at Two Instances in Time for an Impact Velocity of 800 m/s

Figure 5.15 presents the temperature and stress state distribution for all the constituents at the Hugoniot state generated from an 800 m/s impact. Recognize the distributions are for whole grains and not just the grain surfaces, since sintering would only require the surfaces of the grains to melt. The most probable temperature of the

granular network is between 550 and 900 K. Once again, this is dependent on the type of material and therefore the assigned EOS.

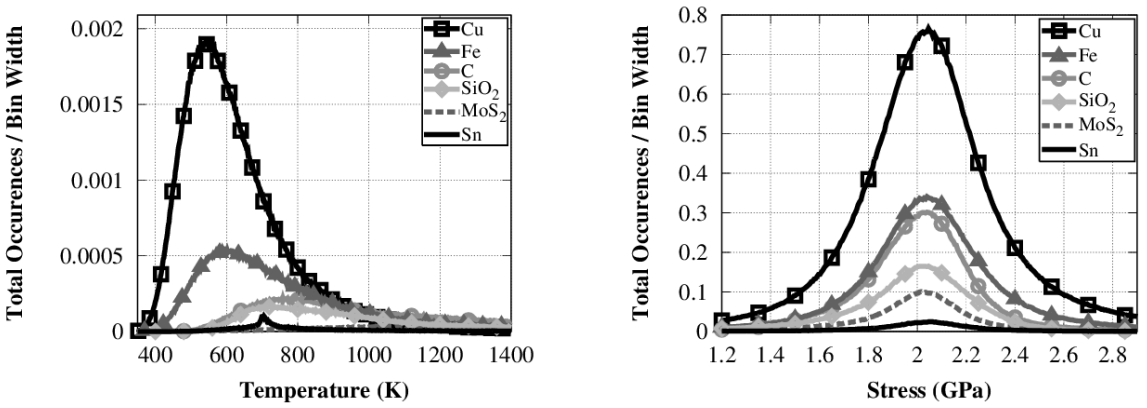

a) Temperature distribution at Hugoniot state b) Stress of the material at Hugoniot state

Figure 5.15 Temperature and Stress Distributions of the Total Powder at the Hugoniot State for an Impact Velocity of 800 m/s

5.4 Stress-Strain Analysis

Another method of determining accurate experiments and simulations is analyzing the stress strain power law relationships of heterogeneous materials. For granular materials, the strain rate is proportional to stress raised to the first power [18]. Figure 5.15 shows non-dimensional results on a log, log plot for scaling of strain rate in various granular materials compared to the experimental results of this report. The equation used to find the strain rate is:

$$\dot{\varepsilon} = \frac{\rho_o U_p^2}{\sigma \Delta t}, \tag{5.10}$$

where ρ_o is the initial bulk density (g/cm^3) of the material, U_P is the particle velocity (km/s), σ is the Hugoniot stress (GPa), and the Δt is the rise time (sec) defined as the asymptotic value of the particle velocity at the interface of the material and backer plate divided by the slope at the middle leading edge of the wave [8, 42, 59]. The non-dimensionality of the plots were determined from the following equations:

$$\frac{\dot{\varepsilon} d}{\sqrt{v_f}\, C_{FD}}, \tag{5.11}$$

$$\frac{\sigma}{v_f^2 (\rho_o C^2)_{FD}}, \tag{5.12}$$

with d defined as the particle diameter (μm), v_f is the volume fraction, C is the sound speed (km/s), and *FD* denotes fully dense materials. The materials used in comparison to the experimental results are polyurethane foam [60], glass [61], sugar [62], TiO_2 [63], and WC [59].

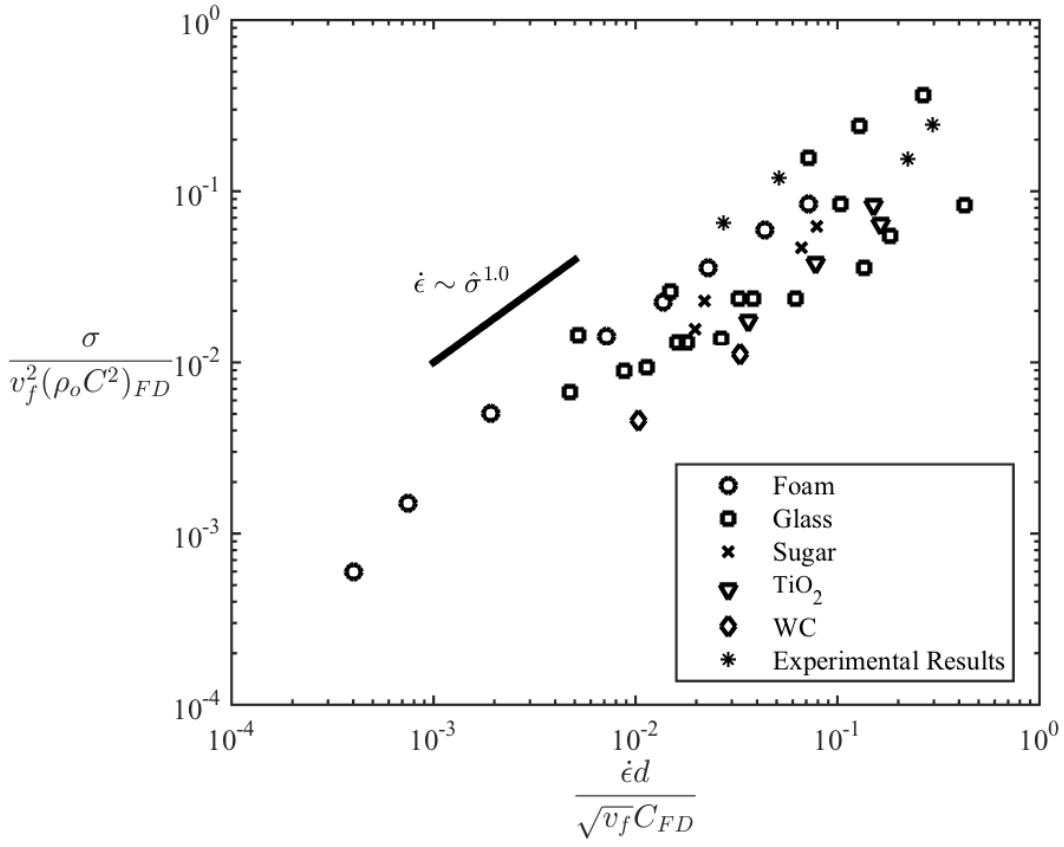

Figure 5.16 Swegle-Grady Stress Strain Power Law Relationship for Brittle Heterogeneous Materials

As is noticed from figure 5.16, the experimental results are clustered together on the graph due to the fact that only a small range of impact velocities were tested. However, sand does fall in this regime where the experimental results are located in this figure [42], suggesting that the experiment validated the models and the simulations.

Figure 5.17 is similar to figure 5.16, however it only includes simulated data from this document: Marquette brake pad, Georgia Tech, and Cambridge. Notice the strain rate is related to the stress to the first power, which was seen for other granular, heterogeneous materials in figure 5.16.

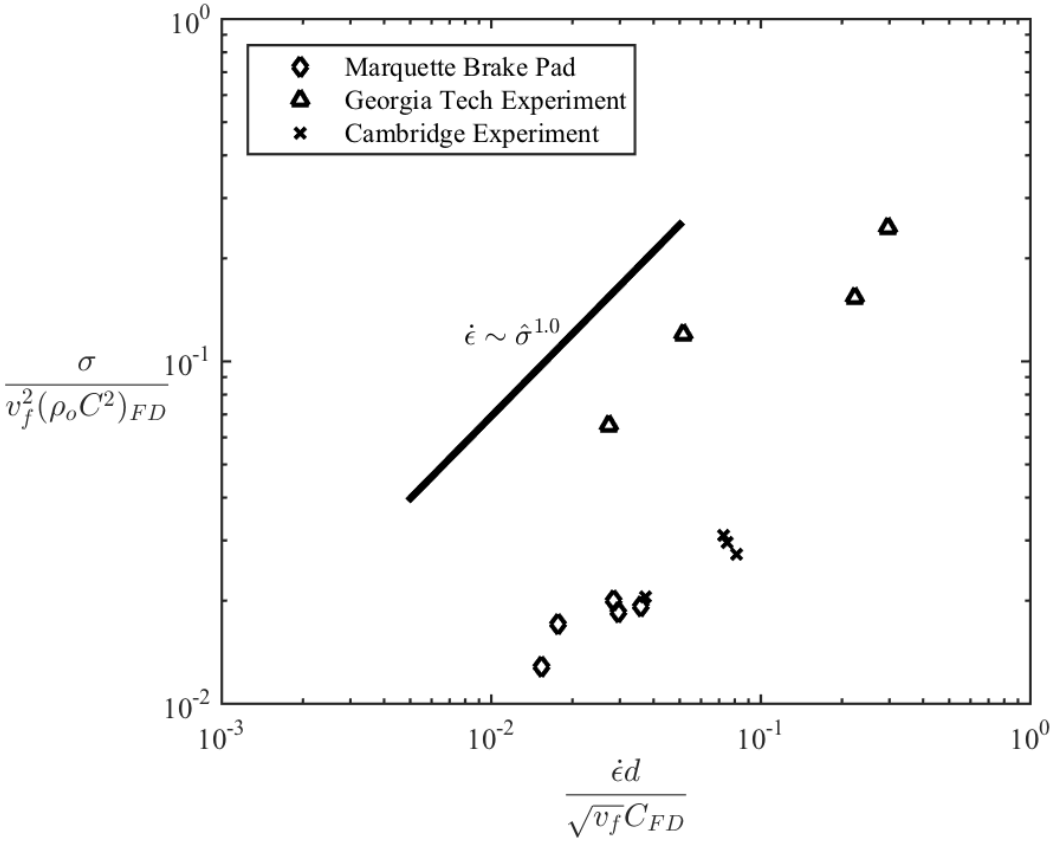

Figure 5.17 Swegle-Grady Stress Strain Power Law Relationship for the Three Case Study Simulated Results

Notice that for even non-brittle materials like the brake-pad powder, which consisted of mainly the ductile material copper, the relationship is still apparent. Although this seems to be true with heterogeneous materials that do not experience a phase change during shock loading, the possibility in future work being completed for water saturated sand as well as possible ice sand mixtures might change this relationship seen from the three case studies presented.

VI. FUTURE WORK

Data for water-saturated sand was not acquired for being able to setup simulations. However, in this section, there will be a discussion on how water-saturated sand can be setup and how the three case studies and results from those studies can be further used to provide information about a different heterogeneous mixture.

It is hypothesized that small amounts of water saturation provide a less stiff Hugoniot response than that of just dry sand. Fully saturated sand would believe to give a more stiff dynamic response, as grains would not be allowed to slide as freely in comparison to less water saturated sand. The understood benefit in a less stiff response is related directly to the energy dissipated during the shock event. An example is discussed on this behavior below.

For setting up sand with water molecules and/or ice crystals, a different method is utilized in occupying the computational domain in comparison to sand. Spheres were inserted into the spaces occupied by air until a desired mass percentage of water is achieved. Fully saturated sand is typically around 22% by mass of the sand sample, as seen in various experiments of water-saturated sand [1, 16, 17]. The number of spheres needed is determined from trial and error methods by calculating the approximate mass of the water from the volume of the spheres.

Figure 6.1 presents two computational domain images of water-saturated sand. On the left, the figure presents a sliced 5 x 5 x 5 mm, fully water saturated sand sample (22% by mass) and on the right shows the side of the sample in the direction of shock from left to right.

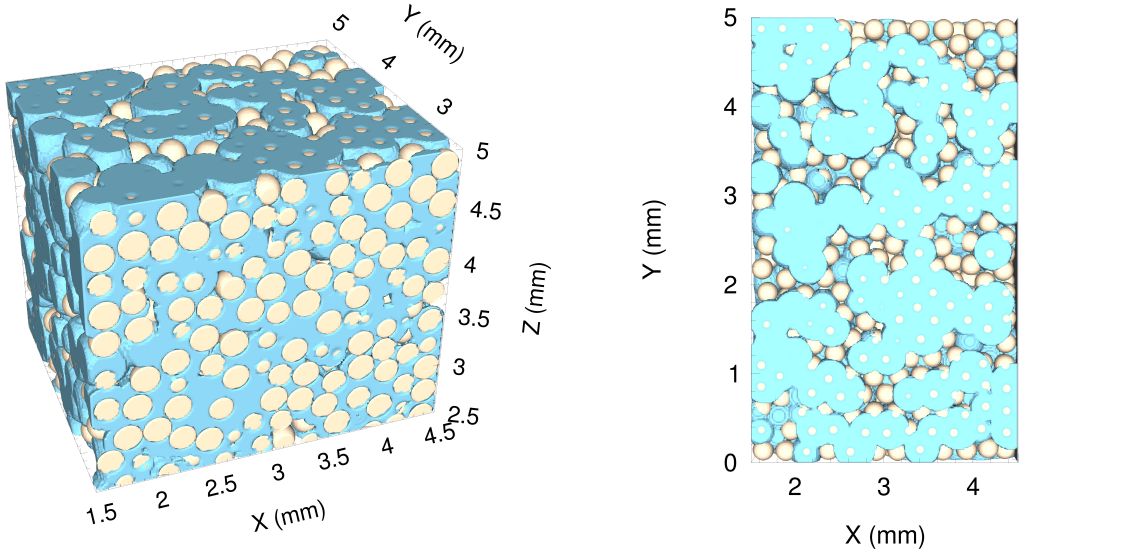

a) Three-Dimesnional Slice

b) Two-Dimesnional Side View (Direction of shock from left to right)

Figure 6.1 Water Saturated Sand Computational Setup

The sand used is builder's sand at 190 microns in diameter has a volume fraction of 53% or 1.453 g/cc and is for demonstration purposes only. Notice that even for fully water saturated sand samples, void is still present in the mixture, which is consistent with the given example numbers.

The water-saturated sand was simulated utilizing the same geometry of the Georgia Tech case study to give slight insight into the dynamic bulk response of the materials. The model was setup by placing a block of water in the sand to present no void at all to simulate fully water-saturated sand. However the results in regards to the Hugoniot were stiffer than experimental Hugoniots. Before the spheres were the shape of choice, tetrahedrons were inserted into the computational domain, but when the sand approached a fully saturated configuration, slip bands and planes were created by the

jagged edges of the tetrahedrons. For future setups, it would be viable to test how the material behaves with these two configurations.

The method for inserting ice is the same as for inserting water with the only difference being specified by the equation of state. This is not a very good assumption, since when water freezes, the material expands and changes the mass percentage that is in the sand mixture. However, the method used for CTH is the method that would be utilized in experiments, as one would measure the mass percentage of liquid water in the sand mixture and then freeze that mixture before impacting the material. The only inaccuracy that is left is in the geometry of the ice, as the current model does not take into account the expansion of frozen water.

The simulation methods for the Marquette Brake Pad Case study discussed in this document could be used to gain insight into how water-saturated and ice sand behaves under dynamic loading. Specifically, the method used in understanding the distribution of particles at the Hugoniot state for the Marquette Brake Pad experiments could be between the water or ice and quartz particles. It would be of interest to the shock physics community to know water and sand grains interact and give a rough surface-to-surface pressure and temperature at the Hugoniot state for various impact velocities. Selecting the right equation of state for water and ice would be crucial in gaining histogram information. Due to the high impedance mismatch between water and quartz, the hypothesis for the results would appear bi-modal, as water would allow some sand particles to reach the Hugoniot state and others would dissipate that stress and “heat” to keep particles below the bulk Hugoniot.

In regards to further development into simulating the dynamic response for water-saturated sand with the use of three-dimensional mesoscale simulations, the Georgia Tech case study provides a great sample experimental setup, and also a base for allowing a comparison to dry sand to be made. By saturating Oklahoma sand with the same setup allows for consistency to carry over when analyzing water-saturated sand and validating simulations.

Release of water-saturated sand in comparison to the Cambridge Dry Sand release experiments would involve a deeper understanding of how to utilize the Riemann integral to develop an isentropic release path for material that no longer utilizes only a Mie-Grüneisen equation of state. However, with the presented information for the Cambridge case study provides a start for determining the release path for more complicated heterogeneous mixtures; not only for water-saturated sand but also for ice sand mixtures.

The following is a list of additional future ideas to further develop and provide to the shock physics community and the shock physics group at Marquette University:

- A better understanding of release in materials and how to utilize and setup better planar shock experiments to measure this release in heterogeneous materials. This would not only pertain to dry sand but also water-saturated and ice sand mixtures as well. This would involve a decent amount of research into developing analytical models for the release states of these mixtures.
- Further utilizing mesoscale simulations to model three-dimensional high velocity dart penetration experiments.

- Implementations of the explosives package in CTH to simulate the dynamic response of sand and water-saturated sand on a rigid plate, and compare the response.
- The Marquette Visualization Lab – Although this type of visualization might not offer insight into the specific state variables at the Hugoniot state, utilizing peridynamic formulations such as Sandia's Peridigm or EMU in conjunction with this resource at Marquette University not only would help visualize how grains interact with one another, but also make others aware of the type of research that is done in the Marquette Shock Physics group. For example, Peridigm utilizes Paraview, a Sandia National Labs viewing software that is also utilized by the Marquette Visualization lab.
- Implementation of the open source code iSALE as well as developing further collaborations with the Imperial College of London. Although iSALE limits the number of tracers, the number of materials, requires a number of cells instead of a defining the domain with spatial coordinates, and does not possess very sophisticated strength models, the code is allowed to be adapted at the user's discretion. The changing of the source code for CTH cannot be completed.

There are various other research ideas that could be involved in future work, but the above suggestions are the most feasible and could further progress the work of the case studies in this document. Furthermore, with the interest from the Air-Force Office of Scientific Research that helped to fund this research would like to further develop these

mesoscale simulations to not only model dry sand but other complicated granular heterogeneous materials. The multi-dimensional visualization techniques provided by CTH play an important part in explaining the overall picture of the dynamic loading of granular materials.

VII. CONCLUSIONS

It is quite remarkable how well mesoscale simulations model planar shock experiments, when the scale of the models are ten times smaller than the experimental setups. By using a simple Mie Grüneisen equation of state in conjunction with an elastic, perfectly plastic Von-Mises strength model, the mesoscale simulations were validated in comparison to experiments, making the study of these mesoscale simulations quite relevant.

This document presented new experimental results for the planar shock dynamic compaction of heterogeneous granular materials. From the simulations of these three different experiments, various factors were determined in order to model planar shock experiments. Overall, the sensitivity analysis by Dr. Borg presented a foundation in which to setup three-dimensional simulations, by understanding the different micro and macro scale variables that needed to be considered, such as yield strength, grain morphology, and volume fraction.

From the Georgia Tech experiments for Oklahoma Sand, it was determined that for an accurate and validated mesoscale model, sliding, or the inexistence of shear at the sign of welding of particles needed to be included. The welding of the particles created too stiff of a response and therefore did not portray the experimental data. Additionally, the experimental setup designed and utilized by Dr. Naresh Thadhani and Dr. Gregory Kennedy could potentially help to setup future experiments to be able to compare the dynamic bulk response of dry and water saturated Oklahoma sand.

The Marquette Brake Pad Experiments helped to develop histograms to observe individual particles at the Hugoniot state and how not all particles are at the shocked state. This could be further implemented to water-saturated sand in observing the surface-to-surface interaction like that of the brake pad powder constituents.

Further research needs to be accomplished to develop methods for determining the isentropic release path for water-saturated sand. The Cambridge dry sand release experiments provides a foundation for this analysis, but by going one step further from a basic Mie Grüneisen equation of state and diving into SESAME or ANEOS tables, and developing isentropic release paths with the equations for more complicated heterogeneous mixtures would prove to be useful for the shock physics community.

Mesoscale simulations provide information about the processes seen in planar shock experiments that real-life experiments cannot. Vis-à-vis, as was seen with the three case studies presented in this document, the validation of the simulated information could not have been validated without the experimental results. In moving forward, the conjunction of mesoscale simulations with planar shock experiments can now be expanded to characterize more complicated heterogeneous granular compositions, which will further benefit the academic and overall shock physics community.

VIII. REFERENCES

[1] Arley, M., Gardou, M., Fleureau, J. M., 2010, "Dynamic Behavior of Dry and Water-Saturated Sand Under Planar Shock Conditions", International Journal of Impact Engineering, **37**pp. 1.

[2] England, J. L., 2013, "Statistical Physics of Self-Replication", American Institute of Physics - the Journal of Chemical Physics, **139**.

[3] LaJeunesse, J., Borg, J. P., and Martin B., 2014, "Simulating the Planar Shock Response of Concrete", Dynamic Behavior of Materials, Volume 1 Proceedings of the 2014 Annual Conference on Experimental and Applied Mechanics, Springer International Publishing, **1,** pp. 369-377.

[4] Tsembelis, K., Proud, W.G., Vaughan, B.A.M., 2002, "The Behavior of Sand under Shock Wave Loading: Experiments and Simulations", n.p. .

[5] Borg, J. P., Morrissey, M. P., Perich, C. A., 2013, "In Situ Velocity and Stress Characterization of a Projectile Penetrating a Sand Target: Experimental Measurements and Continuum Simulations", International Journal of Impact Engineering, **51**(0) pp. 23-35.

[6] Matsumoto, G., 2003, "Bioterrorism: Anthrax Powder: State of the Art".

[7] Parab, N. D., Claus, B., Hudspeth M.C., 2014, "Experimental Assessment of Fracture of Individual Sand Particles at Different Loading Rates", International Journal of Impact Engineering, **68**pp. 8-14.

[8] Brown, J.L., Vogler, T.J., Chabildas, L.C., 2007, "Shock Response of Dry Sand", Sandia National Laboratories, Albuquerque NM; Livermore, CA.

[9] Braithwaite, C. H., Perry, J. I., Taylor, N. E., 2013, "Behavior of Sand during Release from a Shocked State", Applied Physics Letters, **103**(154103).

[10] Trunin, R. F., Simakov, G. V., and Podurets, M. A., 1971, "Compression of Porous Quartz by Strong Shock Waves", Izvestiya, Earth Physics, **2**pp. 33-39.

[11] Simakov, G. V., and Trunin R.F., 1990, "Shockwave Compression of Ultraporous Silica", Izvestiya, Earth Physics, **26**(11) pp. 952.

[12] Vildanov, V. G., Gorshkov, M. M., Slobodenjukov V.M., 1996, "Shock Compression of Low Initial Density Quartz at Pressures Up to 100 GPa", American Institute of Physics.

[13] Wackerle, J., 1962, "Shock Wave Compression of Quartz", Journal of Applied Physics, **33**(4) pp. 922-937.

[14] Anderson, W. W., "Properties of Shocked Aerogel", Lunar and Planetary Science, **28**(1833) .

[15] Boade, R. R., 1970, "Principal Hugoniot, Second-Shock Hugoniot, and Release Behavior of Pressed Copper Powder", Journal of Applied Physics, **41**(11) pp. 4542-4551.

[16] Chapman, D. J., Tesembelis, K., and Proud, W. G., 2006, "The Behavior of Water Saturated Sand under Shock-Loading", SEM Annual Conference and Exposition, Anonymous.

[17] Dianov, M. D., Zlatin, N. A., Mochalov, S. M., 1977, "Shock Compressibility of Dry and Water-Saturated Sand", American Institute of Physics, pp. 207.

[18] Grady, D. E., 1996, "Shock Wave Properties of Brittle Solids", American Institute of Physics, **370**pp. 20.

[19] Herrmann, W., 1969, "Constitutive Equation for the Dynamic Compaction of Ductile Porous Materials", Journal of Applied Physics, **40**(6) pp. 2490-2499.

[20] Jos, G.M. van der Grinten, and Marinus, E. H. v. D., 1987, "Strain and Pore Pressure Propagation in a Water-Saturated Porous Medium", Journal of Applied Physics, **62**(12) pp. 4682.

[21] Linde, R. K., Seaman, L., and Schmidt, D. N., 1972, "Shock Response of Porous Copper, Iron, Tungsten, and Polyurethane", Journal of Applied Physics, **43**(8) pp. 3367-3375.

[22] Fox, D. M., and Lee, J. S., 2014, "The Influence of Water, Dry Sand, and Unsaturated Sand Constitutive Behavior on the Blast Response of a Rigid Target", International Journal of Impact Engineering, **65**pp. 163-173.

[23] Braun, C. A., Schumaker, M. G., Rice, J., "Comparison of Static and Dynamic Powder Compaction: Experiment and Simulation".

[24] Schumaker, M. G., Borg, J. P., Thadhani, N. N., 2014, "Mesoscale Simulations of Dry Sand", Dynamic Behavior of Materials, Volume 1 Proceedings of the 2014 Annual Conference on Experimental and Applied Mechanics, Springer International Publishing, pp. 379-388.

[25] Trunin, R.F., 1998, "Shock Compression of Condensed Materials", Cambridge University Press, Cambridge, UK, pp. 167.

[26] Collins, G., and Davison, T., 2006, "iSALE (impact-SALE) A multi-material extension of the SALE hydrocode (Simplified Arbitrary Lagrangian Eulerian)".

[27] Amsden, A., Ruppel, H., and Hirt, C., 1980, "iSALE: A Simplified ALE Computer Program for Fluid Flow at All Speeds", LANL, LA-8095, Los Alamos, New Mexico.

[28] McGlaun, J. M., Thompson S.L., and Elrick M.G., 1990, "CTH-A Three-Dimensional Shock-Wave Physics Code", International Journal of Impact Engineering, **10**pp. 351-360.

[29] Crawford, D.A., and et al., 2014, "CTH User's Manual and Input Instructions, Version 11.0, CTH Development Project", Sandia National Laboratories, Albuquerque New Mexico.

[30] Copper, P.W., 1996, "Explosives Engineering", Wiley-VHC, New York, NY, pp. 480.

[31] Wilkins, M.L., 1999, "Computer Simulation of Dynamic Phenomena", Springer-Verlag, Berlin, Heidelberg, New York, pp. 239.

[32] Department of Defense, 2013, "ERDC DOD Supercomputing Resource Center", **2015**(January 27).

[33] Borg, J. P., and Vogler, T. J., 2009, "Aspects of Simulating the Dynamic Compaction of a Granular Ceramic", Modeling and Simulation in Materials Science and Engineering, **45**.

[34] Saltelli, A., Ratto, M., Andres, T., 2008, "Global Sensitivity Analysis: The Primer", pp. 304.

[35] Hashemi, J., and Smith, W.F., 2010, "Foundations of Materials Science and Engineering", McGraw Hill, New York, NY, pp. 1068.

[36] Meyers, M.A., 1992, "Shock Wave and High-Strain Rate Phenomena in Materials", CRC Press, pp. 1184.

[37] Asay, J.R., Shahinpoor, M., 1993, "High-Pressure Shock Compression of Solids", Springer-Verlag, New York, NY, pp. 393.

[38] Bird, B., Stewart, W., and Lightfoot, E., 2007, "Transport Phenomena", John Wiley & Sons, Inc., New York, New York, pp. 900.

[39] Meyers, M.A., 1994, "Dynamic Behavior of Materials", John Wiley & Sons, Toronto, Canada, pp. 668.

[40] Thompson S.L., 1990, "ANEOS Analytic Equations of State for Shock Physics Codes Input Manual", Sandia National Laboratory, Albuquerque New Mexico.

[41] LASL Data Center for Dynamic Material Properties, 1980, "Los Alamos Scientific Laboratory (LASL) Shock Hugoniot Data", University of California Press, Berkeley and Los Angeles, CA; London , England.

[42] Vogler, T. J., Borg, J. P., and Grady, D. E., 2012, "On the Scaling of Steady Structured Waves in Heterogeneous Materials", Journal of Applied Physics, **112**(12) pp. 123507.

[43] Barker, L. M., "VISAR Vs. PDV", pp. 1.

[44] Anonymous 2014, "Special use Sensors - Manganin Pressure Sensor".

[45] Braun, C. A., 2011, "One-Dimensional Strain Initiated by Rapid Compaction of a Heterogeneous Granular Mixture Consisting of Cu, Fe, SiO2, C, MoS2, and Sn", Marquette University.

[46] Torquato, S., Truskett, T. M., and Debenedetti, P. G., 2000, "Is Random Close Packing of Spheres Well Defined?", Physical Review Letters,

[47] Cheng S., and Grest G.S., 2013, "Molecular Dynamics Simulations of Evaporation-Induced Nanoparticle Assembly", Journal of Chemical Physics, **138**.

[48] Gourdin, W.H., 1986, "Progress in Material Science", pp. 39-80.

[49] The Boeing Company, March, 1969, "Hugoniot Equation of State of Mylar".

[50] Rosenberg, Z., June, 1981, "The use of Manganin Gages in Shock Reverberation Experiments", Journal of Applied Physics, **52**(6) pp. 4000-4002.

[51] Rosenberg, Z., Yaziv, D., and Partom, Y., January 25, 1980, "Calibration of Foil-Like Manganin Gages in Planar Shock Wave Experiments", Journal of Applied Physics, **51**(7) pp. 3702-3705.

[52] Lee, L. M., 1995, "Calibration of Thin-Foil Manganin Gages in Alox Materials", American Physical Society - Shock Compression of Condensed Matter.

[53] Kerley, G.I., December 1999, "Equations of State for Composite Materials", Kerley Publishing Services, KPS99-4.

[54] Anonymous "Online Materials Information Resource, MatWeb", (February 14).

[55] Root, S., and Assay J.R., "Loading Path and Rate Dependence of Inelastic Deformation: X-Cut Quartz", Journal of Applied Physics, **106** (5).

[56] Jordan, J. L., and Baer, M. R., 2012, "Mixture Model for Determination of Shock Equation of State", Journal of Applied Physics, **111** (8) pp. 083516.

[57] Asay, J. R., 1975, "Shock and Release Behavior in Porous 1100 Aluminum", Journal of Applied Physics, **46**(197).

[58] Kraus, R. G., Chapman D.J., Proud W.G., 2009, "Hugoniot and Spall Strength Measurements of Porous Aluminum", Journal of Applied Physics, **105**.

[59] Vogler, T. J., Lee, M. Y., and Grady, D. E., 2007, "Static and Dynamic Compaction of Ceramic Powders", International Journal of Solids and Structures, **44**(2) pp. 636-658.

[60] Zaretsky, E., Asaf, Z., Ran, E., 2012, "Impact Response of High Density Flexible Polyurethane Foam", International Journal of Impact Engineering, **39**(1) pp. 1-7.

[61] Neal, W. D., Chapman, D. J., and Proud, W. G., 2012, "Shock-Wave Stability in Quasi-Mono-Disperse Granular Materials", The European Physical Journal of Applied Physics, **57**(3).

[62] Davison, L., Horie, Y., Shahinpoor, M., 1997, Springer New York, pp. 23-61.

[63] Dunbar, E., Graham, R. A., Holman, G. T., 1994, "Time-Resolved Pressure Measurements in Chemically Reacting Powder Mixtures", AIP Conference Proceedings, **309**(1) pp. 1303.